Title: Perturbation of *de novo* lipogenesis hinders MERS-CoV assembly and release, but not the biogenesis of viral replication organelles

Authors:

M. Soultsioti[1], A.W.M. de Jong[2], N. Blomberg[3], A. Tas[1], M. Giera[3], E. J. Snijder[1]#, M. Barcena[2]#

Affiliations:

1. Molecular Virology Laboratory, Center for Infectious Diseases (LUCID), Leiden University Medical Center
2. Section Electron Microscopy, Department of Cell and Chemical Biology, Leiden University Medical Center
3. Center for Proteomics and Metabolomics, Leiden University Medical Center

#Corresponding author: m.barcena@lumc.nl or e.j.snijder@lumc.nl

Keywords:

coronavirus, TOFA, 2-BP, acetyl-CoA carboxylase, lipid metabolism, palmitoylation

Abstract (*max 250 words*)

Coronaviruses hijack host cell metabolic pathways and resources to support their replication. They induce extensive host endomembrane remodeling to generate viral replication organelles and exploit host membranes for assembly and budding of their enveloped progeny virions. Because of the overall significance of host membranes, we sought to gain insight into the role of host factors involved in lipid metabolism in cells infected with Middle East respiratory syndrome coronavirus (MERS-CoV). We employed a single-cycle infection approach in combination with pharmacological

inhibitors, biochemical assays, lipidomics, light and electron microscopy. Pharmacological inhibition of acetyl-CoA carboxylase (ACC) and fatty acid synthase (FASN), key host factors in *de novo* fatty acid biosynthesis, led to pronounced inhibition of MERS-CoV particle release. Inhibition of ACC led to a profound metabolic switch in Huh7 cells, altering their lipidomic profile and inducing lipolysis. However, despite the extensive changes induced by the ACC inhibitor, the biogenesis of viral replication organelles remained unaffected. Instead, ACC inhibition appeared to affect the trafficking and post-translational modifications of the MERS-CoV envelope proteins. Electron microscopy revealed an accumulation of nucleocapsids in early budding stages, indicating that MERS-CoV assembly is adversely impacted by ACC inhibition. Notably, inhibition of palmitoylation resulted in similar effects, while supplementation of exogenous palmitic acid reversed the compound's inhibitory effects, possibly reflecting a crucial need for palmitoylation of the MERS-CoV Spike and Envelope proteins for their role in virus particle assembly.

Importance (*max 150 words***)**

Middle East respiratory syndrome coronavirus (MERS-CoV) is the etiological agent of a zoonotic respiratory disease of limited transmissibility between humans. However, MERS-CoV is still considered a high-priority pathogen and is closely monitored by WHO due to its high lethality rate of around 35% of laboratory-confirmed infections. Like other positive-strand RNA viruses, MERS-CoV relies on the host cell's endomembranes to support various stages of its replication cycle. However, in spite of this general reliance of MERS-CoV replication on host cell lipid metabolism, mechanistic insights are still very limited. In our study, we show that pharmacological inhibition of acetyl-CoA carboxylase (ACC), a key enzyme in the

host cell's fatty acid biosynthesis pathway, significantly disrupts MERS-CoV particle assembly without exerting a negative effect on the biogenesis of viral replication organelles. Furthermore, our study highlights the potential of ACC as a target for the development of host-directed antiviral therapeutics against coronaviruses.

Introduction

Viruses rely heavily on the host cell's metabolic and biosynthetic capabilities to support their replication cycle. As such, the manipulation of host cell metabolic pathways has been a long-standing research topic for a range of evolutionary divergent DNA and RNA virus families, such as herpesviruses, flaviviruses, and picornaviruses, as reviewed in (1, 2). In the case of coronaviruses, virus-host interactions related to cellular metabolism constituted a rather poorly studied area until the emergence of severe acute respiratory syndrome coronavirus-2 (SARS-CoV-2) in December 2019 (3, 4). Since then, several studies have highlighted that coronaviruses, like other virus families, hijack host metabolic pathways to support various stages of their replication (5-12).

During their replication cycle (reviewed in (13-15)), coronaviruses, including the highly pathogenic SARS-CoV, SARS-CoV-2, and Middle East respiratory syndrome coronavirus (MERS-CoV), hijack intracellular membranes to accommodate viral RNA synthesis (16-23) and the assembly of enveloped progeny virions (21, 24-27). Briefly, after coronavirus entry and release of the positive-strand RNA genome (gRNA) into the cytoplasm, the gRNA is translated into two large replicase polyproteins. These are autoproteolytically processed by internally encoded viral proteases, resulting in the generation of 16 viral nonstructural proteins (nsps) that engage in viral RNA synthesis and a range of virus-host interactions. All

77 coronaviruses studied so far induce the formation of a perinuclear network of
78 modified membrane structures that derive from the endoplasmic reticulum (ER). This
79 network includes double-membrane vesicles (DMVs), paired or convoluted
80 membranes (CMs), and double-membrane spherules (DMSs), which are collectively
81 referred to as the coronavirus replication organelle (RO) (18, 20). DMVs are the most
82 abundant structures and constitute the primary site of viral genome replication and
83 generation of subgenomic (sg) mRNAs (20, 21). A molecular pore complex was
84 found to span the DMV's double membrane, thus connecting the DMV interior with
85 the cytosol (28-30) and presumably constituting a gateway for viral RNA export. In
86 the cytoplasm, the sg mRNAs are translated, giving rise to the viral structural and
87 accessory proteins. In parallel, part of the newly synthesized gRNAs associate with
88 Nucleocapsid (N) proteins to form ribonucleoprotein (RNP) complexes, which
89 constitute the nucleocapsid substructures that will be packaged in the virus particle.
90 During their synthesis, the viral envelope proteins associate with membranes of the
91 secretory pathway, into which the nucleocapsid buds. Progeny virions acquire their
92 envelope from intracellular membranes that primarily originate from the ER-Golgi
93 intermediate compartment (ERGIC) (21, 26), after which they are released from the
94 infected cell. Historically, viral egress was thought to occur via the biosynthetic
95 secretory pathway (31), but recent evidence suggests that coronaviruses may (also)
96 employ parts of the lysosomal pathway (27, 32-34).
97 Given the overall significance of host cell lipids and membranes in pivotal stages of
98 coronavirus replication, it is not surprising that recent genome-wide association
99 studies (GWAS) have identified host factors involved in fatty acid biosynthesis/*de*
100 *novo* lipogenesis (DNL) and cholesterol biosynthesis to be important for the
101 replication of SARS-CoV-2 and other coronaviruses (35-37). Host factors identified

102 included the sterol regulatory element-binding proteins (SREBP-1 and SREBP-2)
103 and SREBP cleavage-activating protein (SCAP), which are major regulators of DNL
104 and cholesterol biosynthesis (38). A prior study also implicated SREBPs in MERS-
105 CoV replication, potentially in DMV formation (6). Due to the impact of the SARS-
106 CoV-2 pandemic and the urgency of developing broad-spectrum antiviral
107 therapeutics, the potential of enzymes of the DNL pathway as drug targets for
108 intervention and treatment of COVID-19 has been explored, yielding some promising
109 results (10, 39, 40). It should however be noted that, while most studies on
110 coronavirus replication so far have uncovered a general reliance on DNL-related
111 pathways, further mechanistic insights remain scarce.
112 The aim of our present study was to explore the role of DNL in the MERS-CoV
113 replication cycle. Our results show that inhibition of acetyl-CoA carboxylase (ACC)
114 disrupts the assembly of infectious MERS-CoV progeny, while the formation of viral
115 replication organelles remains unaffected. The inhibitory effect on virus assembly
116 could be partially reversed by supplementation with exogenous palmitic acid,
117 possibly reflecting a need for palmitoylation of the MERS-CoV Spike (S) and
118 Envelope (E) proteins. Our results also highlight the potential of ACC as a target for
119 the development of host-directed antiviral treatment.
120

121 **Results**

122 ***MERS-CoV infection increases gene expression of host factors involved in***
123 ***DNL***

124 *De novo* lipogenesis begins with the generation of acetyl-CoA from citrate through
125 the activity of ATP citrate lyase (ACLY) (Figure 1A). Acetyl-CoA is further
126 carboxylated by the rate-limiting enzyme ACC, leading to the production of malonyl-

127 CoA. Malonyl-CoA then serves as a substrate for the fatty acid synthase enzyme
128 (FASN), leading to the generation of saturated fatty acids (such as myristic acid,
129 palmitic acid, and stearic acid) that can be utilized in post-translational modifications
130 (e.g., myristoylation and palmitoylation), phospholipid synthesis, and fatty acid
131 catabolism (β-oxidation) (Figure 1A).
132 First, we investigated if MERS-CoV infection altered the gene expression levels of
133 various host factors involved in DNL (*ACLY, ACC, FASN, SCD-1*), phospholipid
134 synthesis (*DGAT1*), formation of lipid droplets (LDs) (*ADRP*), or fatty acid oxidation
135 pathways (*CPT1*α and *ACOX*). To this end, Huh7 cells were infected with MERS-
136 CoV at a high multiplicity of infection (MOI 5). At 12 h p.i., cells were lysed and
137 mRNA expression was analyzed by RT-qPCR. This timepoint was chosen as it
138 combined abundant viral RNA synthesis with the early phase of virus assembly and
139 release. Under such conditions, we observed an increase in the mRNA levels of host
140 factors involved in initial steps of the DNL pathway, such as the rate-limiting
141 enzymes ACC and FASN, and an increase in the mRNA levels of ADRP (Figure 1B).
142 From the fatty acid oxidation pathway factors that were analyzed, only ACOX was
143 moderately increased. We then evaluated the expression of ACC and FASN on a
144 protein level by Western blot analysis (Figure 1C). Despite the observed alterations
145 in mRNA levels, a clear change in the protein abundance of ACC and FASN could
146 not be detected. However, this result may be attributed to the limited sensitivity of the
147 assay or a reduced turn-over of these proteins. During high energy requirement, the
148 activity of ACC is regulated via its phosphorylation by AMP-activated protein kinase
149 (AMPK), which leads to inactivation of ACC. In this context, we also evaluated the
150 levels of phospho-ACC by Western blot, but did not observe any changes (Figure
151 1C), indicating that ACC's activity is not inhibited in MERS-CoV-infected cells.

152 Our combined observations suggested that host factors of the DNL branch of lipid
153 metabolism are transcriptionally upregulated in MERS-CoV-infected cells.
154
155 ***DNL inhibition does not affect viral RNA synthesis but impairs a later step in***
156 ***the MERS-CoV replication cycle***
157 To investigate the role of DNL pathways in coronavirus replication, we made use of
158 the fast-acting and potent small-molecule inhibitor 5-(tetradecyloxy)-2-furoic acid
159 (TOFA), which blocks the activity of ACC and thus the synthesis of fatty acids
160 (Figure 1A) (41, 42). Our aim was to explore whether pharmacological inhibition of
161 ACC would influence viral replication, in particular the steps that directly involve host
162 cell endomembranes: replication organelle formation and assembly of progeny
163 virions. For this, Huh7 cells were infected with MERS-CoV at MOI 5 and treated with
164 non-cytotoxic concentrations of TOFA (Figure S1A) from 1 h p.i. onward, following
165 removal of the virus inoculum. Total intracellular RNA and cell culture supernatant
166 were collected at 16 h p.i. Interestingly, compared to the DMSO-treated control, no
167 changes were observed in the levels of intracellular viral RNA (as detected by RT-
168 qPCR) when infected Huh7 (Figure 2A) or MRC5 (Figure 2B) cells were treated with
169 TOFA. However, by plaque assay we measured a 4-log reduction in infectious viral
170 progeny released from Huh7 cells (Figure 2C) and an approximately 2.5-log
171 reduction in the case of MRC5 cells (Figure 2D). When using TVB-2640, a small-
172 molecule inhibitor that blocks the activity of FASN downstream of ACC (Figure 1A),
173 similar trends were again observed in Huh7 cells, with the intracellular viral RNA
174 levels remaining unaltered while the infectious progeny titers were reduced
175 approximately 30-fold upon compound treatment (Figure 2E and 2F). Taken

176 together, our data indicated that the DNL branch of lipid metabolism plays a proviral
177 role in MERS-CoV replication.
178 When MERS-CoV-infected Huh7 cells were treated with TOFA, the amount of
179 infectious viral progeny was found to slowly increase from undetectable at 12 h p.i. to
180 about 10^3 PFU/ml by 16 h p.i. Although the viral titers showed an increase over time,
181 a systematic 4-log difference was observed when comparing the vehicle control and
182 the TOFA-treated samples (Figure 2G). Overall, these data led us to conclude that
183 pharmacological inhibition of ACC, without affecting viral RNA synthesis, severely
184 hampered a later step in the coronavirus replication cycle, such as virus assembly,
185 egress, or virus particle infectivity.
186 Because of the significant reduction in extracellular infectious viral progeny following
187 compound treatment, we sought to understand whether the pharmacological
188 inhibition of ACC affected the host cell's secretory pathway, which is involved in
189 virion release. Using a *Gaussia* luciferase reporter assay (43), we observed that
190 TOFA did not affect the integrity of the secretory pathway, while Brefeldin A, a well-
191 characterized protein trafficking inhibitor, strongly inhibited the secretion of *Gaussia*
192 luciferase in the supernatant (Figure 2H). There were no differences in the
193 intracellular levels of *Gaussia* luciferase across all conditions (Figure 2I), which
194 excluded a general effect of TOFA on protein synthesis. Taken together, our data
195 pointed to an intact secretory pathway in the TOFA-treated cells, without a negative,
196 off-target effect of the compound on the cellular translation machinery, suggesting
197 that the reduction in extracellular infectious particles was not due to a virus egress
198 defect.
199
200 ***TOFA alters the host cell lipidomic profile and induces lipolysis***

201 To gain insight into TOFA's impact on host pathways that are relevant for virus
202 assembly and release, uninfected cells were treated with the compound and
203 harvested 12 h post treatment for targeted lipidomics analysis. This revealed that
204 TOFA treatment induced profound changes in the host cell's lipidomic profile,
205 including increased levels of phosphatidylcholine, phosphatidylserine,
206 lysophospholipids, and lipids of the ceramide biosynthetic pathway (Figure S2A).
207 Strikingly, the levels of neutral lipids including triacylglycerols (TG), cholesterol
208 esters (CE) and diacylglycerols (DG) were significantly reduced (Figure S2A), while
209 free fatty acids (FFA) increased. These latter effects strongly suggested a metabolic
210 switch in TOFA-treated cells towards the hydrolysis of triacylglycerols and
211 diacylglycerols into their constituent molecules of acylglycerols and FFAs, a process
212 also known as lipolysis. Lipolysis ultimately results in the degradation of LDs, which
213 constitute the cellular neutral lipid storage compartments (44).
214 To corroborate the above findings, we used immunofluorescence microscopy and LD
215 labeling with BODIPY 493/503, a well-known neutral lipid dye, and observed a
216 reduced amount of LDs in TOFA-treated cells compared to DMSO-treated control
217 cells (Figure S2B). Our results strongly suggested that pharmacological inhibition of
218 ACC and thus FFA synthesis has a broader effect on lipid metabolism than
219 previously described (42) and induces a compensatory shift toward lipolytic
220 pathways. Similar effects were observed in MERS-CoV-infected cells in a time-
221 dependent manner. At 9 h p.i. (8 h after the start of TOFA treatment), lipid droplets
222 were still present at detectable levels in TOFA-treated infected and uninfected cells
223 (Figure 3A and 3B, panels ii), albeit in somewhat reduced amounts in comparison to
224 the DMSO-treated control cells (Figure 3A and 3B, panels i). However, by 12 h p.i.
225 (11 h after the start of TOFA treatment), there was a prominent difference between

226 the DMSO- and TOFA-treated cells (Figure 3A and 3B, compare panels iii and iv),
227 with the abundance of LDs being strongly reduced in the latter. Taken together,
228 TOFA treatment appeared to induce a gradual metabolic rewiring towards lipolytic
229 pathways in both mock-infected and MERS-CoV-infected cells.
230
231 ***Subcellular localization of MERS-CoV structural proteins upon ACC inhibition***
232 Next, we studied whether the trafficking of MERS-CoV envelope proteins was
233 affected by ACC inhibition. To this end, we investigated their subcellular localization
234 by immunofluorescence labeling and confocal microscopy, while using antibodies
235 recognizing well-characterized host marker proteins to visualize specific
236 compartments of the secretory pathway. Specifically, antibodies against S and M or
237 S and E proteins were used for the simultaneous labeling of two of the envelope
238 proteins, while in the same specimens antibodies against PDI, ERGIC-53, or giantin
239 were used to stain the endoplasmic reticulum (ER), ER-Golgi intermediate
240 compartment (ERGIC), and Golgi complex, respectively. As previously reported for
241 other coronaviruses (26, 45, 46), in untreated infected cells, viral envelope proteins
242 co-localized in both ERGIC (Figure S3) and Golgi membranes (Figure 4A-B). After
243 ACC inhibition, limited changes in the intracellular co-localization patterns of the
244 envelope proteins were observed. For example, in the DMSO-treated control cells,
245 the S protein co-localized with the giantin marker in the Golgi complex (white arrows,
246 Figures 4A and 4B, panel i, yellow spots). Post-TOFA treatment, this co-localization
247 was not observed with the same intensity and the signal for both S protein and
248 giantin seemed more dispersed (Figures 4A and 4B, panel ii). Furthermore, while in
249 the untreated control cells E (Figure 4A) or M (Figure 4B) proteins co-localized with
250 giantin (white arrows in Figures 4A and 4B, panel iii, yellow spots), these co-

251 localizations were no longer apparent after TOFA treatment (Figures 4A and 4B,
252 panel iv). In combination, TOFA treatment resulted in a reduced triple co-localization
253 between S and E proteins with the giantin marker (Figure 4A) or S and M proteins
254 with the giantin marker (Figure 4B) (panels v., white arrows, in comparison with
255 panels vi.). Though the changes upon ACC inhibition were limited in nature, they did
256 suggest that viral envelope protein trafficking to the Golgi complex was altered
257 compared to that in untreated MERS-CoV-infected cells.
258
259 ***TOFA treatment affects intracellular processing and trafficking of MERS-CoV***
260 ***envelope proteins***
261 Using Western blot analysis, we further investigated the status of the MERS-CoV
262 structural proteins S, E, M, and N in both extracellular samples (culture supernatants
263 from infected and TOFA-treated cells) as well as cell lysates.
264 Only trace amounts of the N protein could be detected in the supernatant collected
265 from TOFA-treated infected cells (Figure 5A), while the amounts of the three
266 envelope proteins were below the detection limit of our assay. Importantly, this result
267 excluded the possibility that the decrease in viral infectivity titers in supernatants
268 from TOFA-treated cells (Figure 2C) was merely due to the production of non-
269 infectious virus particles.
270 Intracellularly, only the overall levels of N protein remained more or less unaffected
271 at 9 and 12 h p.i. in the presence of TOFA. Decreased levels of full-length (FL) S
272 glycoprotein as well as its S1 and S2 fragments were observed, at 9 h and 12 h p.i.
273 Moreover, after TOFA treatment, we could not detect a second band below the S2
274 fragment, which likely corresponds to the S2′ fragment (47), suggesting a decreased
275 transport of the S protein to the trans-Golgi network where the furin protease

276 responsible for this cleavage is located. We also observed that the E protein
277 consistently migrated slightly faster after compound treatment, again suggesting
278 changes in the protein's post-translational modifications (Figure 5B).
279 The M protein was detectable as the usual double band, indicative of the two
280 different glycosylation states of M (48), migrating around 15-25 kDa (Figure 5B).
281 However, following compound treatment, the blot for the M protein also revealed a
282 smear of products with a higher molecular weight (in the 20-35 kDa range),
283 suggesting a change in the post-translational maturation and/or trafficking of the M
284 protein. The smear disappeared after glycosidase treatment of the cell lysates with
285 PNGase (Figure 5C), confirming that it resulted from a change in the glycosylation
286 status of M, which was likely linked to a disruption of the protein's intracellular
287 trafficking.
288
289 ***Electron microscopy reveals that TOFA treatment interferes with MERS-CoV***
290 ***assembly and release.***
291 Overall, our data confirmed that TOFA treatment caused a major defect in the
292 release of infectious MERS-CoV progeny, and excluded the possibility that large
293 amounts of non-infectious particles were secreted instead. Our subsequent
294 microscopy and biochemical studies pointed towards changes in the post-
295 translational modification and trafficking of all three MERS-CoV envelope proteins,
296 which might disrupt the normal intracellular assembly of new virions.
297 We employed transmission electron microscopy (TEM) to directly visualize the
298 impact of TOFA treatment on the viral replication cycle. Huh7 cells were infected with
299 MERS-CoV at MOI 5 and treated with the compound from 1 h p.i. onward. Cells
300 were fixed at 12 h p.i. and analyzed with TEM. We observed that pharmacological

301 inhibition of ACC did not affect the formation or morphology of virus-induced ROs
302 (DMVs and CMs) in comparison to the vehicle-treated control cells (Figure 6A,
303 panels i and ii), which aligns with our previous data regarding the unaffected
304 intracellular viral RNA levels upon TOFA treatment (Figure 2A). Moreover, while
305 extracellular progeny virions were abundantly found at the plasma membrane of
306 untreated MERS-CoV-infected cells, they were hardly present in the TOFA-treated
307 samples (Figure 6B, panels i. and ii.), in agreement with the strong reduction in
308 progeny virus titers observed when ACC is inhibited (Figure 2B).
309 Our ultrastructural studies further revealed that the consequences of TOFA
310 treatment hindered virus particle assembly. In untreated control samples (Figure 6C),
311 different stages of virion budding could be detected, from early stages in which the
312 nucleocapsid starts to be engulfed by a curved membrane (Figure 6C, panel i and ii)
313 to (nearly) fully budded virions (panel iii), with the latter representing most virions.
314 However, in TOFA-treated samples, the early stages of virus particle assembly were
315 particularly abundant (Figure 6D), with exceptionally large areas containing particles
316 representing this stage (Figure 6D, panels i and ii). This strongly suggested that
317 TOFA treatment interferes with the normal progress towards a fully budded virus
318 particle, leading to an unusual accumulation of nucleocapsids in an initial budding
319 state.
320
321 ***Inhibition of palmitoyltransferase enzymes mimics the effects of ACC***
322 ***inhibition***
323 One of the many end products of the DNL pathway is the fatty acid palmitate.
324 Palmitate, or palmitic acid, plays an important role in various cellular processes: as a
325 signaling molecule, a structural element of various lipids, and by participating in

326 posttranslational modifications, such as protein palmitoylation catalyzed by
327 palmitoyltransferase enzymes (49). Coronavirus S and E proteins contain a
328 conserved C-terminal cysteine-rich region next to their transmembrane domain,
329 which can serve as a palmitoylation substrate (Figure 7A) (50). Previous studies in
330 cells infected with the murine hepatitis (MHV), transmissible gastroenteritis (TGEV),
331 SARS-CoV, and SARS-CoV-2 coronaviruses, have shown that their S proteins are
332 post-translationally palmitoylated (51-58), while the cysteine-rich regions of the E
333 proteins of SARS-CoV, MHV, and infectious bronchitis virus (IBV) were also found to
334 be palmitoylated (59-62). Since there is no experimental data on the palmitoylation
335 status of the MERS-CoV S and E proteins and the potential role of this
336 posttranslational modification in assembly, we initially tested the importance of
337 palmitoyltransferase enzymes for MERS-CoV replication using 2-bromopalmitic acid
338 (2-BP), a small-molecule inhibitor with a broad effect on palmitoyltransferase
339 enzymes (Figure 1A) (63). In an earlier antiviral compound screen (6), 2-BP was
340 shown to inhibit MERS-CoV replication in a multi-cycle experimental setup, but its
341 mechanism of action was not explored. We now employed a single-cycle setup as
342 described above: Huh7 cells were infected with MOI 5, treated with 2-BP from 1 h
343 p.i. onward, and at 16 h p.i. culture supernatants and total intracellular RNA were
344 collected. Interestingly, we observed that inhibition of palmitoyltransferase enzymes
345 induced similar changes as the ACC inhibition (Figure 7B and 7C). Compared to the
346 untreated control, no major changes were observed in the levels of intracellular viral
347 RNA detected by RT-qPCR in cells treated with 2-BP (Figure 7B). However, there
348 was a ~250-fold reduction in the extracellular infectious progeny titers (Figure 7C),
349 aligning with the hypothesis that limited availability of palmitate after DNL inhibition
350 may be partly responsible for the observed assembly impairment.

351

352 ***Addition of exogenous palmitic acid partially rescues assembly and release of***
353 ***MERS-CoV progeny***

354 Based on the possible involvement of palmitoylation defects in the observed
355 disturbances of MERS-CoV assembly, we investigated whether assembly could be
356 restored by supplementing some of the end products of the DNL pathway, such as
357 palmitic acid or oleic acid. To this end, Huh7 cells were infected with MERS-CoV at
358 MOI 5 and from 1 h p.i. onward they were treated with 10 μM TOFA or TOFA
359 supplemented with 100 μM BSA-conjugated palmitic acid or BSA-conjugated oleic
360 acid. A treatment with 100 μM BSA without conjugated fatty acid served as a vehicle
361 control for the fatty acids (Figure 7D). Fatty acid concentrations where chosen based
362 on previous cytotoxicity assays, using concentrations that would not reduce cell
363 viability below 90% (Figures S1E and S1F), thus aiming to avoid potential
364 confounding effects of lipotoxicity-induced cell death. Interestingly, we observed that
365 the addition of exogenous palmitic acid conjugated with BSA partially restored the
366 release of infectious MERS-CoV progeny in the supernatant (by almost 100-fold),
367 while addition of BSA-conjugated oleic acid or BSA alone did not (Figure 7D).
368 Moreover, the effects of TOFA treatment that we had observed at the level of
369 individual envelope proteins (Figure 5) could be partially reversed by addition of
370 palmitic acid, resulting in intracellular protein levels and post-translational
371 modifications that were closer to those seen in samples from untreated infected cells
372 (Figure 7E). Electron microscopy analysis of large EM data sets also revealed an
373 increase in the number of extracellular virions after palmitic acid addition (Figure 7F),
374 while intracellularly there was a significant decrease in the proportion of virions
375 arrested in the early assembly stage (Figure 7G, with representative images

376 provided in Figure S4). In contrast, a quantitative analysis of the abundance of DMVs
377 (Figure 7H) and CMs (Figure 7I) did not reveal significant changes in comparison to
378 the DMSO-treated control, neither upon TOFA treatment nor upon addition of
379 palmitic acid. Overall, our data indicate an important role for palmitic acid during
380 MERS-CoV assembly, potentially involving palmitoylation of the S and E structural
381 proteins.
382

383 **Discussion**

384 Being enveloped positive-strand RNA viruses, coronaviruses depend on the host
385 cell's endomembrane system to facilitate and support their propagation in several
386 ways. They transform intracellular, ER-derived membranes into the ROs that
387 accommodate viral RNA synthesis and hijack membranes of the secretory pathway
388 to generate enveloped virus particles. Due to this extensive involvement of host
389 membranes, lipid metabolism pathways have been implicated in coronavirus
390 replication (5, 6). After the emergence of SARS-CoV-2, several studies touched
391 upon the potential reprogramming of lipid metabolism in the context of coronaviral
392 replication (8, 10, 11, 39), but few mechanistic details were resolved. Here, we report
393 on the importance of lipid homeostasis in MERS-CoV-infected cells for viral
394 propagation to take place, as perturbations of the fatty acid biosynthesis pathway
395 were found to have a strong inhibitory effect, specifically on the assembly and/or
396 release of viral progeny.
397 Due to the extensive remodeling of the ER during coronavirus RO biogenesis, it has
398 been speculated that fatty acid biosynthetic pathways would be activated to fuel the
399 formation of these membrane structures (6, 10). However, our data show that
400 perturbation of DNL does not affect MERS-CoV RNA synthesis or RO biogenesis

401 (Figure 2A, 2B, 2E and 6A), indicating that – contrary to previous speculations - DNL
402 is not among the host cell pathways critically required for coronaviral RO formation
403 (6, 10). Our data are in partial agreement with published literature on SARS-CoV-2.
404 Earlier studies have shown that lipid metabolism pathways, especially anabolic
405 branches such as DNL and not catabolism of fatty acids (like β-oxidation), play a
406 general proviral role in coronavirus replication (6, 10, 39), which is also corroborated
407 by our data when using inhibitors of ACC and FASN.
408 A previous SARS-CoV-2 study (10), using TOFA among other small-molecule
409 inhibitors of the DNL pathway, showed that DNL inhibition impedes SARS-CoV-2
410 replication. However, using immunofluorescence microscopy, Williams et al,
411 observed a change in the intracellular distribution of double-stranded RNA (dsRNA)
412 foci, which was interpreted to represent a change in the formation of viral ROs. In our
413 study with MERS-CoV, such a dsRNA pattern change was not observed (Figure S5),
414 while electron microscopy analyses of large EM data sets showed no alterations in
415 the morphology (Figure 6) or abundance (Figure 7H-I) of viral ROs. These
416 differences could be attributed to technical details of the immunolabeling protocol or
417 the use of different coronavirus species and host cells. Another technical difference
418 was the use of a single-cycle of viral replication setup in our study, in contrast to the
419 multi-cycle approach and longer experimental timeframes applied in most of the
420 previously published studies (6, 10, 39, 64). By using a single-cycle approach, we
421 aimed to synchronize the different steps of the viral cycle (entry, RO formation, peak
422 of viral RNA and protein synthesis, particle assembly) and study them at defined
423 timepoints.
424 Our data indicate that the DNL pathway, and in particular palmitate, one of its end
425 products, plays a role in MERS-CoV particle assembly or maturation (Figure 7)

426 rather than in RO formation. Palmitoylation of the S and E proteins has been
427 reported to be important for the replication of other coronaviruses, like MHV, SARS-
428 CoV, and SARS-CoV-2 (51-62), making it tempting to assume a similar involvement
429 for MERS-CoV. However, palmitoylation of MERS-CoV structural proteins has not
430 been investigated directly, in infected cells or overexpression/virus-like-particle
431 systems. Consequently, the number of palmitoylated cysteines, and their role and
432 position with respect to the transmembrane domain of the MERS-CoV S and E
433 proteins remain unknown.
434 Depending on the coronavirus studied, disruption of palmitoylation seems to have
435 divergent effects on the replication cycle. For example, palmitoylation of the MHV S
436 protein was reported to be necessary for its interaction with the M protein and
437 assembly of virus particles (51), while palmitoylation of the SARS-CoV or SARS-
438 CoV-2 S protein is not required for its interaction with the M protein (53, 55). It is
439 unknown and rather difficult to predict what the importance of palmitoylation of the
440 MERS-CoV envelope proteins might be, since the molecular interactions between
441 coronaviral S and M protein are generally not well defined. In the coronaviruses
442 studied so far, palmitoylation of S and E proteins seems to increase protein stability
443 and to decrease their turnover rate (61, 62). This could also be the case for MERS-
444 CoV, as suggested by the decrease we observed in intracellular S protein levels
445 after ACC inhibition (Figure 5B). Attempts to use a triple-mutated MHV E protein
446 lacking all potentially palmitoylated cysteines to generate virus-like particles (VLPs)
447 or recombinant mutant MHV, resulted in particles incapable of proper assembly and
448 release in both cases (61, 62). Interestingly, this triple-mutated MHV E protein also
449 exhibited faster migration during SDS-PAGE (61), which is in line with our western
450 blot observations after ACC inhibition (Figure 5B) and the partial recovery of the

451 protein's normal migration after addition of palmitic acid (Figure 7E). Besides
452 impacting their stability, another common effect of palmitoylation on the S and E
453 proteins is the influence on their affinity for specific membrane lipid nanodomains
454 (55, 61). Lack of S and E protein palmitoylation might lead to their association with
455 membranes of different lipid composition than what is necessary for efficient
456 assembly, eventually leading to disruption of the regular assembly events. This is
457 partially supported by our immunofluorescence microscopy data, since we observed
458 reduced co-localization of the S and E proteins with a Golgi compartment marker
459 (Figure 4).
460 The most abundant viral envelope protein and a key driver of particle assembly is the
461 M protein, which has not been reported to be palmitoylated, but it is known to be
462 glycosylated on its short N-terminal ectodomain. Upon TOFA treatment, the M
463 protein exhibited differences in its glycosylation pattern (Figure 5B and 5C). Being on
464 the luminal side of the membrane, the glycans decorating the MHV or SARS-CoV M
465 proteins do not seem to have a crucial role in virion assembly and release, nor in M
466 protein interactions with the S and E proteins (65, 66). However, these previous
467 studies have mainly explored the use of mutated M proteins that lacked the specific
468 amino acid residues normally used for glycan conjugation. In our study, following
469 TOFA treatment, we observed M proteins carrying longer, possibly untrimmed,
470 glycan chains. Trimming of glycan chains takes place as proteins progress from the
471 ER to the Golgi complex, as part of the ER's quality control machinery for misfolded
472 proteins. Glycans are further processed, trimmed, and extended during protein
473 trafficking through the Golgi complex, as part of normal glycoprotein maturation (67,
474 68). Thus, the M protein's glycosylation differences observed in our study could
475 signal trafficking issues that lead to delayed or aberrant processing of its (predicted)

476 single N-linked glycan. Although these changes may not affect virus assembly, they
477 are in line with our immunofluorescence microscopy observations regarding the M
478 protein's reduced colocalization with giantin (Figure 4). According to the western blot
479 results (Figure 5C), about half of the total amount of M protein still appears to be
480 properly processed and trafficked, but the impact of the reduced or delayed
481 availability of M protein at the site of virus assembly is difficult to predict.
482 In conclusion, the observed major impairment of the assembly and release of
483 infectious MERS-CoV progeny upon ACC inhibition may well be a multifactorial
484 phenomenon. In our TEM images (Figure 6D), inhibition of the fatty acid synthesis
485 pathway resulted in a striking increase of the number of early assembly/budding
486 events relative to (nearly) fully-formed virus particles. TOFA treatment may affect
487 virus particle assembly by reducing palmitoylation of S and E proteins, which can
488 potentially result in their instability and increased turnover. Simultaneous changes in
489 M protein trafficking may contribute to an overall imbalance in the viral envelope
490 proteins needed for interactions with each other, host lipids, and viral nucleocapsids,
491 ultimately affecting the pace and quality of virion assembly and budding. In addition
492 to its presumed impact on the trafficking and post-translational modification of viral
493 envelope proteins, TOFA treatment may also affect the properties of unidentified
494 host factors that are directly or indirectly involved in coronavirus assembly. This
495 could also contribute to the general disruption of lipid metabolism pathways and the
496 metabolic switch towards lipolytic pathways that we observed in both mock- and
497 MERS-CoV-infected cells (Figure 3 and S3), which could contribute to an
498 unfavorable microenvironment and host membrane composition for efficient virion
499 assembly. The proviral role of *de novo* lipogenesis in MERS-CoV replication also

500 highlights its potential as a target for the development of host-directed antiviral
501 therapeutics against coronaviruses.
502
503 **Materials and Methods**
504 **Cells**
505 Huh7 cells (kindly provided by Dr. Ralf Bartenschlager, Heidelberg University,
506 Germany) and MRC5 cells (purchased from ATCC, CCL-171) were cultured in
507 Dulbecco's Modified Eagle Medium (DMEM) (Lonza) supplemented with 8% (v/v)
508 fetal calf serum (FCS), 100 IU/mL penicillin/streptomycin, 2 mM L-glutamine, and
509 non-essential amino acids, at 37°C and 5% CO_2.
510
511 **Viruses and virus purification**
512 MERS-CoV strain EMC/2012 (NC_019843) (69, 70) was kindly provided by Dr. Ron
513 Fouchier, Erasmus Medical Center Rotterdam, the Netherlands, and working stocks
514 were prepared using Huh7 cells. All work with live MERS-CoV was performed inside
515 a biosafety level 3 facility at Leiden University Medical Center. Virus titrations by
516 plaque assay were performed as described before (71). Huh7 cells were seeded in
517 tissue culture-treated multiwell plates and the next day were infected with serial
518 dilutions of MERS-CoV containing supernatant for 1 h at 37°C. The virus inoculum
519 was removed and replaced by overlay medium containing 1.2% Avicel RC-581 (Cas.
520 No.: 9004-34-6, FMC/IMCD Benelux) in DMEM supplemented with 2% FCS and 100
521 IU/mL penicillin/streptomycin. Cells were incubated for 3 days at 37°C, after which
522 they were fixed with formaldehyde and stained with crystal violet.
523 Virus concentration by ultracentrifuge pelleting through a sucrose cushion (Figure
524 5A) Infected cell culture supernatants were harvested 16 h p.i. and clarified from cell

525 debris by low-speed centrifugation at 1,200 g for 5 min at 4°C. The virus particles
526 were pelleted through a 20% (w/v) sucrose cushion in TES buffer (0.02 M Tris-HCl,
527 1mM EDTA, 0.1 M NaCl, pH 7.4) by centrifugation in an SW41 Ti rotor (Beckman
528 Coulter) for 3.5 h at 30,000 rpm and 4°C. Virus pellets were resuspended overnight
529 in phosphate-buffered saline (PBS) at 4°C, lysed in 100mM Tris-HCl, pH 7.6 and 4%
530 (w/v) sodium dodecyl sulfate (SDS), and used for SDS-PAGE and Western blot
531 analysis.
532
533 **Small-molecule inhibitors**
534 TOFA (5-tetradecyloxy-2-furoic-acid, cat. No.: HY-101068) and TVB-2640
535 (Denifanstat, cat. No.: HY-112829) were purchased from MedChemExpress.
536 2-bromopalmitic acid (2-bromohexadecanoic acid, cat. No: 21604) was purchased
537 from Sigma. Compounds were dissolved in anhydrous DMSO for stock preparation.
538 BSA-conjugated palmitate saturated fatty acid complex (PA) (cat. No.: 29558), BSA-
539 conjugated oleate monounsaturated fatty acid complex (OA) (cat. No. 29557) and
540 BSA control for BSA-fatty acid complexes (cat. No. 29556) were purchased from
541 Cayman Chemicals.
542
543 **Cytotoxicity assays**
544 Cell viability was monitored using CellTiter 96 aqueous non-radioactive cell
545 proliferation reagent (Promega), following the manufacturer's instructions. Cells were
546 seeded in 96-well plates and incubated overnight at 37°C and 5% CO2. On the next
547 day, the cells were treated with serial dilutions of the different compounds in DMEM
548 containing 2% FCS, 100 IU/mL penicillin/streptomycin, 2 mM L-glutamine and non-
549 essential amino acids. Cells were incubated for 22 h, and then 20 ml/well of MTS

550 solution (3-(4,5-dimethylthiazol-2-yl)-5-(3-carboxymethoxyphenyl)-2-(4-sulfophenyl)-
551 2H-tetrazolium) were added. The cells were incubated for 2 h at 37°C, after which
552 the absorbance was measured at 495 nm using the Envision multiplate reader
553 (PerkinElmer). Cell viability was normalized against the DMSO-treated control.
554

555 **Quantitative PCR**

556 Viral RNA in MERS-CoV-infected Huh7 cells was quantified by using RT-qPCR. To
557 this end, samples were collected in Tripure Isolation Reagent (Sigma), intracellular
558 RNA was isolated following the manufacturer's instructions, and RT-qPCR was
559 performed using the Applied Biosystems™ TaqMan Fast™ Virus 1-step Multiplex
560 Master Mix for qPCR (ThermoFisher) with MERS-CoV-specific primers and probes
561 (designed in-house as described before (72)) in a CFX384 Touch RT-PCR detection
562 system (Biorad). For absolute quantification, a standard curve was generated using
563 10-fold serial dilutions of an *in vitro* transcript containing the target sequences,
564 generated using T7 RNA polymerase. The expression of human PGK1 gene
565 (ThermoFisher, TaqMan gene expression Assay VIC-MGB, cat. No. #4448490,
566 assay ID Hs00943178_g1) was used as an internal standard to ensure equal sample
567 loading between conditions.
568 Gene expression analysis for host factors was performed using real-time RT-qPCR
569 with iTaq SYBR Green Supermix (Biorad) in a CFX384 Touch RT-PCR detection
570 system (Biorad). Primer sequences for *ACLY, ACC, FASN, SCD-1, DGAT1, ADRP,*
571 *CPT1a, ACOX* and human β-actin were described elsewhere (6, 73). Quantification
572 was performed by normalizing against the amount of human β-actin mRNA. Fold
573 gene expression changes in MERS-CoV-infected cells relative to mock-infected cells
574 were calculated by using the delta-delta Ct formula ($2^{-\Delta\Delta Ct}$).

575 All oligonucleotide sequences and sources are provided in the Supplementary Table
576 1.
577
578 ***Gaussia* luciferase reporter assay**
579 For monitoring the effect of TOFA on the secretory pathway's activity, Pierce™
580 *Gaussia* luciferase glow assay kit (ThermoFisher, cat. No.: 16160) was used
581 following the manufacturer's instructions. Huh7 cells were seeded in 96-well plates
582 and the next day, they were transfected with 150 ng of a Gaussia luciferase
583 expression plasmid using Lipofectamine 3000 (ThermoFisher) at a 1:3 ratio of DNA
584 to Lipofectamine. At 24 h post transfection, the cell culture supernatant was
585 aspirated, and the cells were treated for 8 h with DMSO, TOFA, or brefeldin A. After
586 incubation with the compounds, the cell culture supernatant containing secreted
587 *Gaussia* luciferase was collected, and the cell monolayer was lysed for detection of
588 intracellular luciferase. The luciferase signal output was measured at 485 nm using
589 an Envision multiplate reader (PerkinElmer).
590
591 **Immunofluorescence microscopy**
592 Huh7 cells were seeded on glass coverslips and left to attach overnight at 37°C and
593 5% CO2. The next day, cells were either mock- or MERS-CoV infected for 9 h or 12
594 h and then fixed with 3% paraformaldehyde. Immunofluorescence labelling was
595 performed as described before (74). In this study, the following antibodies were used
596 for immunofluorescence analyses: human monoclonal antibody against MERS-CoV
597 Spike protein (kindly provided by Dr. Berend Jan Bosch, Utrecht University) (75),
598 rabbit polyclonal anti-MERS-CoV M protein antibody (20, 76), rabbit polyclonal anti-
599 MERS-CoV E protein antibody (ThermoFisher, cat. No.: PA5-143457), rabbit

600 polyclonal anti MERS-CoV N protein antibody (Sino Biological, cat. No.: 40068-
601 RP02), mouse monoclonal anti-dsRNA J2 antibody (Scicons), mouse monoclonal
602 anti-PDI antibody (Enzo Life Sciences, ADI-SPA-891), mouse monoclonal ERGIC-53
603 G1/93 Ab (Enzo Life Sciences/ Alexis Biochemicals, ALX-804-602), mouse
604 monoclonal anti-giantin antibody (Enzo Life Sciences/Alexis Biochemicals, ALX-804-
605 600), BODIPY493/503 (ThermoFisher, cat. No.: D3922). For viral M and E protein
606 labeling, an Alexa-647-conjugated donkey anti-rabbit secondary antibody (Jackson
607 Laboratories, cat. No.: 711-605-152) was used, the S protein labelling was visualized
608 with an Alexa-488-conjugated goat anti-human antibody (ThermoFisher, cat. No.:
609 A11013), while for the N protein labeling an Alexa-488-conjugated goat anti-rabbit
610 secondary antibody (ThermoFisher, cat. No.: A11008) was used. Cellular organelle
611 markers and dsRNA were labelled using a Cy3-conjugated donkey anti-mouse
612 antibody (Jackson Laboratories, cat. No.: 715-165-150). Leica Sp8 confocal and
613 DM6 fluorescence microscopes were used for image acquisition. During confocal
614 image acquisition, laser strength and gain were kept consistent between all samples
615 and conditions. To obtain high-resolution images, an acquisition format of
616 1024x1024 pixels and speed of 400 Hz were selected and kept consistent between
617 samples. Image acquisition settings were chosen to maximally reduce false-positive
618 co-localization signal due to overexposure of the samples.
619 For image processing, Leica Application Suite X version 3.7 software was used. All
620 images were processed in the same manner to increase brightness and contrast for
621 this publication. Raw, unprocessed images are available upon request.
622
623 **Targeted lipidomics analysis**

624 Comprehensive, quantitative shotgun lipidomics was carried out as described in
625 detail elsewhere (77, 78). Briefly, samples were spiked with deuterated internal
626 standards and lipids were extracted using methyl tert-butyl ether. The combined
627 organic extracts were subsequently dried under a gentle stream of nitrogen and the
628 dried extracts were dissolved in methanol:chloroform 1:1 containing 10 mM
629 ammonium acetate. Lipids were then analyzed with a flow injection method at a flow
630 rate of 8 µL/min applying differential ion mobility for lipid class separation and
631 subsequent multiple reaction monitoring in positive and negative electrospray
632 ionization mode. Using the Shotgun Lipidomics Assistant (SLA) software individual
633 lipid concentrations were calculated after correction for sample input and their
634 respective internal standards.
635
636 **Western blot and PNGase assay**
637 After lysis of cells or purified virus particles, obtained as described above, the protein
638 content of samples was quantified using the Pierce BCA protein assay kit
639 (ThermoFisher). Samples were mixed with 4x Laemmli sample buffer, incubated at
640 96°C for 5 min, and separated using SDS-polyacrylamide gel electrophoresis (SDS-
641 PAGE). Post separation, the proteins were transferred to Amersham Hybond-LFP
642 0.45 µm PVDF blotting membrane (Cytiva) using the semidry Trans-Blot Turbo
643 Transfer System (Biorad). For the E protein, Amersham Hybond-LFP 0.2 µm PVDF
644 blotting membrane was used instead. The membranes were blocked for 1 h at room
645 temperature. For ACC and FASN, 5% bovine serum albumin (BSA) in TBS with
646 0.05% Tween-20 (TBST) was used as a blocking buffer, while for viral proteins 1%
647 casein in PBS with 0.05% Tween-20 (PBST) was used instead. Membranes were

648 incubated with primary antibodies overnight in 2.5% BSA in TBST or 0.5% casein in
649 PBST respectively.
650 Antibodies used in this study were: ACC (Cell Signaling Technology, cat.no.: #3662),
651 phospho-ACC (Ser79) (Cell Signaling Technology, cat.no.: #3661), FASN (Cell
652 Signaling Technology, cat.no.: #3180), rabbit polyclonal anti-MERS-CoV S1 antibody
653 (ThermoFisher, cat. No.: PA5-119581), rabbit polyclonal anti-MERS-CoV S2
654 antibody (ThermoFisher, cat. No.: PA5-81788), rabbit polyclonal anti-MERS-CoV M
655 protein antibody (20, 76), rabbit polyclonal anti-MERS-CoV E protein antibody
656 (ThermoFisher, cat. No.: PA5-143457), rabbit polyclonal anti-MERS-CoV N protein
657 antibody (Sino Biological, cat. No.: 40068-RP02), mouse monoclonal anti-β-actin
658 antibody (Sigma, cat. No.: A5316), GAPDH (14C10) (Cell Signaling Technology,
659 cat.no.: #2118). Following primary antibody incubation, membranes were incubated
660 with a secondary antibody: biotin-conjugated anti-mouse IgG (Thermo Fisher
661 Scientific, cat.no.: 31800) or anti-rabbit IgG (Thermo Fisher Scientific, cat.no.:
662 A16033). After 1 h incubation at room temperature, the membranes were incubated
663 for 1 h with a tertiary Cy3-conjugated anti-biotin antibody (Jackson Laboratories,
664 cat.no.: 200-162-211). Protein bands were visualized using an Alliance Q9 advanced
665 imaging system (Uvitec).
666 For the PNGase assay, the PNGase F kit (New England Biolabs, cat. no.: P0704)
667 was used according to the manufacturer's instructions with a few modifications. The
668 protocol for denaturing conditions was followed and the glycoprotein denaturing
669 buffer was added directly to samples lysed with 4x Laemmli Sample Buffer. The
670 samples were denatured by heating at 100°C for 10 min, they were briefly placed on
671 ice and then centrifuged for 10 sec. GlycoBuffer, 10% NP-40 and H_2O were added to
672 the denatured protein lysate according to NEB's protocol. The reaction mixture was

673 incubated for 1 h at 37°C and then directly subjected to SDS-PAGE and Western
674 blotting.
675
676 **Electron microscopy**
677 Cells were fixed with 1.5% (vol/vol) glutaraldehyde in 0.1 M cacodylate buffer (pH
678 7.4) for 30 min at room temperature, and then stored overnight at 4°C before being
679 exported from the BSL3 facility. Then, the samples were first stained with OsO_4 at
680 4°C for 1 h and subsequently at room temperature with 1% (w/v) uranyl acetate in
681 Milli-Q water for 1 h, with washing steps with 0.1 M cacodylate buffer in between.
682 After a washing step with Milli-Q water, the samples were dehydrated in increasing
683 concentrations of ethanol (70%, 80%, 90%, 100%), embedded in epoxy resin (LX-
684 112, Ladd Research), and polymerized at 60°C. Sections were collected on mesh-
685 100 copper EM grids covered with a carbon-coated Pioloform layer, and poststained
686 with 7% (w/v) uranyl acetate and Reynold's lead citrate.
687 The samples were examined in a Tecnai12 BioTwin or a Twin transmission electron
688 microscope, equipped with an Eagle 4k CCD camera (Thermo Fisher Scientific) or a
689 OneView 4k high-frame rate CMOS camera (Gatan), respectively. For the
690 quantifications, mosaic images of large areas were generated using automatically
691 collected overlapping images (pixel size 2 nm) that were subsequently combined in
692 composite images, as described in (79).. A minimum of 3 large mosaic images from
693 at least 2 different EM grids were analyzed per condition, each one including ~10-25
694 cells and DMVs and virus particles were manually annotated and CM regions
695 delineated using Aperio Imagescope software (Leica). On average, each of these
696 large areas contained ~1,900 DMVs, as well as ~3,000 virus particles in different
697 stages of assembly. The latter were classified based on their assembly stage:

698 particles in early-stage assembly were defined as those with a budding envelope
699 forming a crescent smaller than a semi-circle, whereas virus particles with a budding
700 envelope forming a crescent larger than a semi-circle or appearing fully budded were
701 assigned to the late-stage assembly class. The perimeter of cells and nuclei in these
702 regions was also manually delineated to calculate densities per μm^2 of cytoplasm.
703

704 **Statistical analysis**

705 Data are represented as mean ± standard deviation (SD) of at least two biological
706 replicates. Statistical significance was calculated using unpaired Student's t-test,
707 when comparing two groups, or two-way ANOVA and applying multiple comparison
708 corrections, when comparing multiple groups. Statistical significance is denoted with
709 asterisks as: * $p<0.05$, ** $p< 0.01$, *** $p< 0.001$, **** $p< 0.0001$. Prism version 10
710 (GraphPad Software Inc.) was used to perform all statistical analyses and
711 calculations.
712

713 **Software**

714 Geneious Software (version 10.2) was used for the alignment of partial S and E
715 protein sequences from selected coronaviruses. The list of viruses was selected
716 based on available information from published literature on S and E protein
717 palmitoylation modifications of these viruses. Their protein sequences were then
718 compared to the sequences of MERS-CoV S and E proteins. The following
719 accession numbers were used: MERS-CoV (NC_019843), SARS-CoV (NC_004718)
720 SARS-CoV-2 (NC_045512), MHV (AY700211), TGEV (AJ271965), IBV
721 (NC_001451), HCoV-229E (NC_001451).

722 Figure annotations (Fig. 5, 7E and S1) and schematics (Fig. 1A) were created using
723 Adobe Illustrator 2025.
724
725 **Supplementary data**
726 Available as a separate file.
727
728 **Data availability**
729 Raw lipidomics data used to generate and support the conclusions of Figure S2A are
730 available in a public repository (Mendeley Data, doi: 10.17632/sknp5pwj5y.1).
731
732 **Acknowledgements**
733 The authors would like to thank Patrick Wanningen, Heidi de Gruyter, and Tim
734 Dalebout for technical assistance, Annelies Boonzaier-van der Laan for confocal
735 microscopy assistance, Nadya Urakova and Quinten Ducarmon for helpful
736 discussions. The study was partially funded by the European Union's Horizon 2020
737 research and innovation program under the Marie Skłodowska-Curie grant
738 agreement number 813343 (H2020-MSCA-ITN-813343-INITIATE), and by the
739 Netherlands Organization for Scientific Research (grant NWO-OCENW.M.21.339).
740
741 **Author Contribution**
742 Study design, M.S., M.B., and E.J.S.; methodology, M.S., A.W.M.J., and N.B.;
743 investigation, M.S., A.W.M.J., N.B., and A.T.; formal analysis, M.S. and M.B.;
744 resources, M.G., M.B., and E.J.S.; writing – original draft, M.S., M.B., and E.J.S.;
745 writing - editing and final approval, M.S., A.W.M.J., A.T., N.B., M.G., M.B., and
746 E.J.S.; supervision, M.B. and E.J.S.; funding acquisition, M.B. and E.J.S.

Conflict of Interest

The authors have no conflict of interest to declare.

References

1. Goodwin CM, Xu S, Munger J. 2015. Stealing the Keys to the Kitchen: Viral Manipulation of the Host Cell Metabolic Network. Trends in Microbiology 23:789-798.
2. Sanchez EL, Lagunoff M. 2015. Viral activation of cellular metabolism. Virology 479-480:609-618.
3. Zhou P, Yang X-L, Wang X-G, Hu B, Zhang L, Zhang W, Si H-R, Zhu Y, Li B, Huang C-L, Chen H-D, Chen J, Luo Y, Guo H, Jiang R-D, Liu M-Q, Chen Y, Shen X-R, Wang X, Zheng X-S, Zhao K, Chen Q-J, Deng F, Liu L-L, Yan B, Zhan F-X, Wang Y-Y, Xiao G-F, Shi Z-L. 2020. A pneumonia outbreak associated with a new coronavirus of probable bat origin. Nature 579:270-273.
4. Zhu N, Zhang D, Wang W, Li X, Yang B, Song J, Zhao X, Huang B, Shi W, Lu R, Niu P, Zhan F, Ma X, Wang D, Xu W, Wu G, Gao GF, Tan W. 2020. A Novel Coronavirus from Patients with Pneumonia in China, 2019. N Engl J Med 382:727-733.
5. Yan B, Chu H, Yang D, Sze K-H, Lai P-M, Yuan S, Shuai H, Wang Y, Kao RY-T, Chan JF-W, Yuen K-Y. 2019. Characterization of the Lipidomic Profile of Human Coronavirus-Infected Cells: Implications for Lipid Metabolism Remodeling upon Coronavirus Replication. Viruses 11:73.
6. Yuan S, Chu H, Chan JF-W, Ye Z-W, Wen L, Yan B, Lai P-M, Tee K-M, Huang J, Chen D, Li C, Zhao X, Yang D, Chiu MC, Yip C, Poon VK-M, Chan CC-S, Sze K-H, Zhou J, Chan IH-Y, Kok K-H, To KK-W, Kao RY-T, Lau JY-N, Jin D-Y, Perlman S, Yuen K-Y. 2019. SREBP-dependent lipidomic reprogramming as a broad-spectrum antiviral target. Nature Communications 10:120.
7. Codo AC, Davanzo GG, Monteiro LdB, de Souza GF, Muraro SP, Virgilio-da-Silva JV, Prodonoff JS, Carregari VC, de Biagi Junior CAO, Crunfli F, Jimenez Restrepo JL, Vendramini PH, Reis-de-Oliveira G, Bispo dos Santos K, Toledo-Teixeira DA, Parise PL, Martini MC, Marques RE, Carmo HR, Borin A, Coimbra LD, Boldrini VO, Brunetti NS, Vieira AS, Mansour E, Ulaf RG, Bernardes AF, Nunes TA, Ribeiro LC, Palma AC, Agrela MV, Moretti ML, Sposito AC, Pereira FB, Velloso LA, Vinolo MAR, Damasio A, Proença-Módena JL, Carvalho RF, Mori MA, Martins-de-Souza D, Nakaya HI, Farias AS, Moraes-Vieira PM. 2020. Elevated Glucose Levels Favor SARS-CoV-2 Infection and Monocyte Response through a HIF-1α/Glycolysis-Dependent Axis. Cell Metabolism 32:437-446.e5.
8. Dias SSG, Soares VC, Ferreira AC, Sacramento CQ, Fintelman-Rodrigues N, Temerozo JR, Teixeira L, Nunes da Silva MA, Barreto E, Mattos M, de Freitas CS, Azevedo-Quintanilha IG, Manso PPA, Miranda MD, Siqueira MM, Hottz ED, Pao CRR, Bou-Habib DC, Barreto-Vieira DF, Bozza FA, Souza TML, Bozza PT. 2020. Lipid droplets fuel SARS-CoV-2 replication and production of inflammatory mediators. PLoS Pathog 16:e1009127.
9. Zhang Y, Guo R, Kim SH, Shah H, Zhang S, Liang JH, Fang Y, Gentili M, Leary CNO, Elledge SJ, Hung DT, Mootha VK, Gewurz BE. 2021. SARS-CoV-2 hijacks folate and one-carbon metabolism for viral replication. Nature Communications 12:1676.
10. Williams CG, Jureka AS, Silvas JA, Nicolini AM, Chvatal SA, Carlson-Stevermer J, Oki J, Holden K, Basler CF. 2021. Inhibitors of VPS34 and fatty-acid metabolism suppress SARS-CoV-2 replication. Cell Rep 36:109479.
11. Farley SE, Kyle JE, Leier HC, Bramer LM, Weinstein JB, Bates TA, Lee J-Y, Metz TO, Schultz C, Tafesse FG. 2022. A global lipid map reveals host dependency factors conserved across SARS-CoV-2 variants. Nature Communications 13:3487.

12. Greene KS, Choi A, Chen M, Yang N, Li R, Qiu Y, Lukey MJ, Rojas KS, Shen J, Wilson KF, Katt WP, Whittaker GR, Cerione RA. 2023. Inhibiting Glutamine Metabolism Blocks Coronavirus Replication in Mammalian Cells. bioRxiv doi:10.1101/2023.09.27.559756:2023.09.27.559756.
13. Wang Y, Grunewald M, Perlman S. 2020. Coronaviruses: An Updated Overview of Their Replication and Pathogenesis, p 1-29. *In* Maier HJ, Bickerton E (ed), Coronaviruses: Methods and Protocols doi:10.1007/978-1-0716-0900-2_1. Springer US, New York, NY.
14. Malone B, Urakova N, Snijder EJ, Campbell EA. 2022. Structures and functions of coronavirus replication-transcription complexes and their relevance for SARS-CoV-2 drug design. Nat Rev Mol Cell Biol 23:21-39.
15. Steiner S, Kratzel A, Barut GT, Lang RM, Aguiar Moreira E, Thomann L, Kelly JN, Thiel V. 2024. SARS-CoV-2 biology and host interactions. Nat Rev Microbiol doi:10.1038/s41579-023-01003-z.
16. Gosert R, Kanjanahaluethai A, Egger D, Bienz K, Baker SC. 2002. RNA replication of mouse hepatitis virus takes place at double-membrane vesicles. J Virol 76:3697-708.
17. Snijder EJ, van der Meer Y, Zevenhoven-Dobbe J, Onderwater JJ, van der Meulen J, Koerten HK, Mommaas AM. 2006. Ultrastructure and origin of membrane vesicles associated with the severe acute respiratory syndrome coronavirus replication complex. J Virol 80:5927-40.
18. Knoops K, Kikkert M, Worm SHEVD, Zevenhoven-Dobbe JC, Van Der Meer Y, Koster AJ, Mommaas AM, Snijder EJ. 2008. SARS-Coronavirus Replication Is Supported by a Reticulovesicular Network of Modified Endoplasmic Reticulum. PLoS Biology 6:e226.
19. Maier HJ, Neuman BW, Bickerton E, Keep SM, Alrashedi H, Hall R, Britton P. 2016. Extensive coronavirus-induced membrane rearrangements are not a determinant of pathogenicity. Scientific Reports 6:27126.
20. Snijder EJ, Limpens RWAL, De Wilde AH, De Jong AWM, Zevenhoven-Dobbe JC, Maier HJ, Faas FFGA, Koster AJ, Bárcena M. 2020. A unifying structural and functional model of the coronavirus replication organelle: Tracking down RNA synthesis. PLOS Biology 18:e3000715.
21. Klein S, Cortese M, Winter SL, Wachsmuth-Melm M, Neufeldt CJ, Cerikan B, Stanifer ML, Boulant S, Bartenschlager R, Chlanda P. 2020. SARS-CoV-2 structure and replication characterized by in situ cryo-electron tomography. Nature Communications 11:5885.
22. Cortese M, Lee J-Y, Cerikan B, Neufeldt CJ, Oorschot VMJ, Köhrer S, Hennies J, Schieber NL, Ronchi P, Mizzon G, Romero-Brey I, Santarella-Mellwig R, Schorb M, Boermel M, Mocaer K, Beckwith MS, Templin RM, Gross V, Pape C, Tischer C, Frankish J, Horvat NK, Laketa V, Stanifer M, Boulant S, Ruggieri A, Chatel-Chaix L, Schwab Y, Bartenschlager R. 2020. Integrative Imaging Reveals SARS-CoV-2-Induced Reshaping of Subcellular Morphologies. Cell Host & Microbe 28:853-866.e5.
23. Ogando NS, Dalebout TJ, Zevenhoven-Dobbe JC, Limpens R, van der Meer Y, Caly L, Druce J, de Vries JJC, Kikkert M, Bárcena M, Sidorov I, Snijder EJ. 2020. SARS-coronavirus-2 replication in Vero E6 cells: replication kinetics, rapid adaptation and cytopathology. J Gen Virol 101:925-940.
24. Tooze J, Tooze S, Warren G. 1984. Replication of coronavirus MHV-A59 in sac- cells: determination of the first site of budding of progeny virions. Eur J Cell Biol 33:281-93.
25. Klumperman J, Locker JK, Meijer A, Horzinek MC, Geuze HJ, Rottier PJ. 1994. Coronavirus M proteins accumulate in the Golgi complex beyond the site of virion budding. Journal of Virology 68:6523-6534.
26. Stertz S, Reichelt M, Spiegel M, Kuri T, Martínez-Sobrido L, García-Sastre A, Weber F, Kochs G. 2007. The intracellular sites of early replication and budding of SARS-coronavirus. Virology 361:304-315.
27. Ghosh S, Dellibovi-Ragheb TA, Kerviel A, Pak E, Qiu Q, Fisher M, Takvorian PM, Bleck C, Hsu VW, Fehr AR, Perlman S, Achar SR, Straus MR, Whittaker GR, de Haan CAM, Kehrl J, Altan-

843 Bonnet G, Altan-Bonnet N. 2020. β-Coronaviruses Use Lysosomes for Egress Instead of the
844 Biosynthetic Secretory Pathway. Cell 183:1520-1535.e14.
845 28. Wolff G, Limpens R, Zevenhoven-Dobbe JC, Laugks U, Zheng S, de Jong AWM, Koning RI,
846 Agard DA, Grünewald K, Koster AJ, Snijder EJ, Bárcena M. 2020. A molecular pore spans the
847 double membrane of the coronavirus replication organelle. Science 369:1395-1398.
848 29. Zimmermann L, Zhao X, Makroczyova J, Wachsmuth-Melm M, Prasad V, Hensel Z,
849 Bartenschlager R, Chlanda P. 2023. SARS-CoV-2 nsp3 and nsp4 are minimal constituents of a
850 pore spanning replication organelle. Nature Communications 14:7894.
851 30. Huang Y, Wang T, Zhong L, Zhang W, Zhang Y, Yu X, Yuan S, Ni T. 2024. Molecular
852 architecture of coronavirus double-membrane vesicle pore complex. Nature 633:224-231.
853 31. Tooze J, Tooze SA, Fuller SD. 1987. Sorting of progeny coronavirus from condensed secretory
854 proteins at the exit from the trans-Golgi network of AtT20 cells. J Cell Biol 105:1215-26.
855 32. Scherer KM, Mascheroni L, Carnell GW, Wunderlich LCS, Makarchuk S, Brockhoff M, Mela I,
856 Fernandez-Villegas A, Barysevich M, Stewart H, Suau Sans M, George CL, Lamb JR, Kaminski-
857 Schierle GS, Heeney JL, Kaminski CF. 2022. SARS-CoV-2 nucleocapsid protein adheres to
858 replication organelles before viral assembly at the Golgi/ERGIC and lysosome-mediated
859 egress. Science Advances 8:eabl4895.
860 33. Miura K, Suzuki Y, Ishida K, Arakawa M, Wu H, Fujioka Y, Emi A, Maeda K, Hamajima R,
861 Nakano T, Tenno T, Hiroaki H, Morita E. 2023. Distinct motifs in the E protein are required
862 for SARS-CoV-2 virus particle formation and lysosomal deacidification in host cells. J Virol
863 97:e0042623.
864 34. Pearson GJ, Mears HV, Broncel M, Snijders AP, Bauer DLV, Carlton JG. 2024. ER-export and
865 ARFRP1/AP-1-dependent delivery of SARS-CoV-2 Envelope to lysosomes controls late stages
866 of viral replication. Sci Adv 10:eadl5012.
867 35. Daniloski Z, Jordan TX, Wessels HH, Hoagland DA, Kasela S, Legut M, Maniatis S, Mimitou EP,
868 Lu L, Geller E, Danziger O, Rosenberg BR, Phatnani H, Smibert P, Lappalainen T, tenOever BR,
869 Sanjana NE. 2021. Identification of Required Host Factors for SARS-CoV-2 Infection in Human
870 Cells. Cell 184:92-105.e16.
871 36. Wang R, Simoneau CR, Kulsuptrakul J, Bouhaddou M, Travisano KA, Hayashi JM, Carlson-
872 Stevermer J, Zengel JR, Richards CM, Fozouni P, Oki J, Rodriguez L, Joehnk B, Walcott K,
873 Holden K, Sil A, Carette JE, Krogan NJ, Ott M, Puschnik AS. 2021. Genetic Screens Identify
874 Host Factors for SARS-CoV-2 and Common Cold Coronaviruses. Cell 184:106-119.e14.
875 37. Schneider WM, Luna JM, Hoffmann HH, Sánchez-Rivera FJ, Leal AA, Ashbrook AW, Le Pen J,
876 Ricardo-Lax I, Michailidis E, Peace A, Stenzel AF, Lowe SW, MacDonald MR, Rice CM, Poirier
877 JT. 2021. Genome-Scale Identification of SARS-CoV-2 and Pan-coronavirus Host Factor
878 Networks. Cell 184:120-132.e14.
879 38. Eberlé D, Hegarty B, Bossard P, Ferré P, Foufelle F. 2004. SREBP transcription factors: master
880 regulators of lipid homeostasis. Biochimie 86:839-848.
881 39. Chu J, Xing C, Du Y, Duan T, Liu S, Zhang P, Cheng C, Henley J, Liu X, Qian C, Yin B, Wang HY,
882 Wang RF. 2021. Pharmacological inhibition of fatty acid synthesis blocks SARS-CoV-2
883 replication. Nat Metab 3:1466-1475.
884 40. Duan X, Tang X, Nair MS, Zhang T, Qiu Y, Zhang W, Wang P, Huang Y, Xiang J, Wang H,
885 Schwartz RE, Ho DD, Evans T, Chen S. 2021. An airway organoid-based screen identifies a
886 role for the HIF1α-glycolysis axis in SARS-CoV-2 infection. Cell Reports 37:109920.
887 41. McCune SA, Harris RA. 1979. Mechanism responsible for 5-(tetradecyloxy)-2-furoic acid
888 inhibition of hepatic lipogenesis. J Biol Chem 254:10095-101.
889 42. Halvorson DL, McCune SA. 1984. Inhibition of fatty acid synthesis in isolated adipocytes by 5-
890 (tetradecyloxy)-2-furoic acid. Lipids 19:851-6.
891 43. Tannous BA. 2009. Gaussia luciferase reporter assay for monitoring biological processes in
892 culture and in vivo. Nat Protoc 4:582-91.

893 44. Grabner GF, Xie H, Schweiger M, Zechner R. 2021. Lipolysis: cellular mechanisms for lipid
894 mobilization from fat stores. Nature Metabolism 3:1445-1465.
895 45. Lim KP, Liu DX. 2001. The Missing Link in Coronavirus Assembly: Retention of the avian
896 coronavirus infectious bronchitis virus envelope protein in the pre-Golgi compartments and
897 physical interaction between the envelope and membrane proteins. Journal of Biological
898 Chemistry 276:17515-17523.
899 46. Venkatagopalan P, Daskalova SM, Lopez LA, Dolezal KA, Hogue BG. 2015. Coronavirus
900 envelope (E) protein remains at the site of assembly. Virology 478:75-85.
901 47. Millet JK, Whittaker GR. 2014. Host cell entry of Middle East respiratory syndrome
902 coronavirus after two-step, furin-mediated activation of the spike protein. Proceedings of
903 the National Academy of Sciences 111:15214-15219.
904 48. Perrier A, Bonnin A, Desmarets L, Danneels A, Goffard A, Rouille Y, Dubuisson J, Belouzard S.
905 2019. The C-terminal domain of the MERS coronavirus M protein contains a trans-Golgi
906 network localization signal. J Biol Chem 294:14406-14421.
907 49. F SM, Abrami L, Linder ME, Bamji SX, Dickinson BC, van der Goot FG. 2024. Mechanisms and
908 functions of protein S-acylation. Nat Rev Mol Cell Biol 25:488-509.
909 50. J Alsaadi EA, Jones IM. 2019. Membrane Binding Proteins of Coronaviruses. Future Virology
910 14:275-286.
911 51. Thorp EB, Boscarino JA, Logan HL, Goletz JT, Gallagher TM. 2006. Palmitoylations on murine
912 coronavirus spike proteins are essential for virion assembly and infectivity. J Virol 80:1280-9.
913 52. Petit CM, Chouljenko VN, Iyer A, Colgrove R, Farzan M, Knipe DM, Kousoulas KG. 2007.
914 Palmitoylation of the cysteine-rich endodomain of the SARS-coronavirus spike glycoprotein
915 is important for spike-mediated cell fusion. Virology 360:264-74.
916 53. McBride CE, Machamer CE. 2010. Palmitoylation of SARS-CoV S protein is necessary for
917 partitioning into detergent-resistant membranes and cell-cell fusion but not interaction with
918 M protein. Virology 405:139-48.
919 54. Gelhaus S, Thaa B, Eschke K, Veit M, Schwegmann-Wessels C. 2014. Palmitoylation of the
920 Alphacoronavirus TGEV spike protein S is essential for incorporation into virus-like particles
921 but dispensable for S-M interaction. Virology 464-465:397-405.
922 55. Mesquita FS, Abrami L, Sergeeva O, Turelli P, Qing E, Kunz B, Raclot C, Paz Montoya J,
923 Abriata LA, Gallagher T, Dal Peraro M, Trono D, D'Angelo G, van der Goot FG. 2021. S-
924 acylation controls SARS-CoV-2 membrane lipid organization and enhances infectivity. Dev
925 Cell 56:2790-2807 e8.
926 56. Wu Z, Zhang Z, Wang X, Zhang J, Ren C, Li Y, Gao L, Liang X, Wang P, Ma C. 2021.
927 Palmitoylation of SARS-CoV-2 S protein is essential for viral infectivity. Signal Transduct
928 Target Ther 6:231.
929 57. Puthenveetil R, Lun CM, Murphy RE, Healy LB, Vilmen G, Christenson ET, Freed EO, Banerjee
930 A. 2021. S-acylation of SARS-CoV-2 spike protein: Mechanistic dissection, in vitro
931 reconstitution and role in viral infectivity. J Biol Chem 297:101112.
932 58. Li D, Liu Y, Lu Y, Gao S, Zhang L. 2022. Palmitoylation of SARS-CoV-2 S protein is critical for S-
933 mediated syncytia formation and virus entry. J Med Virol 94:342-348.
934 59. Corse E, Machamer Carolyn E. 2002. The Cytoplasmic Tail of Infectious Bronchitis Virus E
935 Protein Directs Golgi Targeting. Journal of Virology 76:1273-1284.
936 60. Liao Y, Yuan Q, Torres J, Tam JP, Liu DX. 2006. Biochemical and functional characterization of
937 the membrane association and membrane permeabilizing activity of the severe acute
938 respiratory syndrome coronavirus envelope protein. Virology 349:264-75.
939 61. Boscarino JA, Logan HL, Lacny JJ, Gallagher TM. 2008. Envelope protein palmitoylations are
940 crucial for murine coronavirus assembly. J Virol 82:2989-99.
941 62. Lopez Lisa A, Riffle Ambere J, Pike Steven L, Gardner D, Hogue Brenda G. 2008. Importance
942 of Conserved Cysteine Residues in the Coronavirus Envelope Protein. Journal of Virology
943 82:3000-3010.

63. Webb Y, Hermida-Matsumoto L, Resh MD. 2000. Inhibition of protein palmitoylation, raft localization, and T cell signaling by 2-bromopalmitate and polyunsaturated fatty acids. J Biol Chem 275:261-70.
64. Yuan S, Yan B, Cao J, Ye Z-W, Liang R, Tang K, Luo C, Cai J, Chu H, Chung TW-H, To KK-W, Hung IF-N, Jin D-Y, Chan JF-W, Yuen K-Y. 2021. SARS-CoV-2 exploits host DGAT and ADRP for efficient replication. Cell Discovery 7:100.
65. de Haan CA, Kuo L, Masters PS, Vennema H, Rottier PJ. 1998. Coronavirus particle assembly: primary structure requirements of the membrane protein. J Virol 72:6838-50.
66. de Haan CA, Smeets M, Vernooij F, Vennema H, Rottier PJ. 1999. Mapping of the coronavirus membrane protein domains involved in interaction with the spike protein. J Virol 73:7441-52.
67. Helenius A, Aebi M. 2004. Roles of N-linked glycans in the endoplasmic reticulum. Annu Rev Biochem 73:1019-49.
68. Moremen KW, Tiemeyer M, Nairn AV. 2012. Vertebrate protein glycosylation: diversity, synthesis and function. Nat Rev Mol Cell Biol 13:448-62.
69. van Boheemen S, de Graaf M, Lauber C, Bestebroer Theo M, Raj VS, Zaki Ali M, Osterhaus Albert DME, Haagmans Bart L, Gorbalenya Alexander E, Snijder Eric J, Fouchier Ron AM. 2012. Genomic Characterization of a Newly Discovered Coronavirus Associated with Acute Respiratory Distress Syndrome in Humans. mBio 3:e00473-12.
70. Zaki AM, van Boheemen S, Bestebroer TM, Osterhaus AD, Fouchier RA. 2012. Isolation of a novel coronavirus from a man with pneumonia in Saudi Arabia. N Engl J Med 367:1814-20.
71. van den Worm SH, Eriksson KK, Zevenhoven JC, Weber F, Züst R, Kuri T, Dijkman R, Chang G, Siddell SG, Snijder EJ, Thiel V, Davidson AD. 2012. Reverse genetics of SARS-related coronavirus using vaccinia virus-based recombination. PLoS One 7:e32857.
72. Ogando NS, Zevenhoven-Dobbe JC, Meer Yvd, Bredenbeek PJ, Posthuma CC, Snijder EJ. 2020. The Enzymatic Activity of the nsp14 Exoribonuclease Is Critical for Replication of MERS-CoV and SARS-CoV-2. Journal of Virology 94:10.1128/jvi.01246-20.
73. van Huizen M, Bloeme - ter Horst JR, de Gruyter HLM, Geurink PP, van der Heden van Noort GJ, Knaap RCM, Nelemans T, Ogando NS, Leijs AA, Urakova N, Mark BL, Snijder EJ, Myeni SK, Kikkert M. 2024. Deubiquitinating activity of SARS-CoV-2 papain-like protease does not influence virus replication or innate immune responses in vivo. PLOS Pathogens 20:e1012100.
74. van der Meer Y, van Tol H, Krijnse Locker J, Snijder Eric J. 1998. ORF1a-Encoded Replicase Subunits Are Involved in the Membrane Association of the Arterivirus Replication Complex. Journal of Virology 72:6689-6698.
75. Widjaja I, Wang C, van Haperen R, Gutiérrez-Álvarez J, van Dieren B, Okba NMA, Raj VS, Li W, Fernandez-Delgado R, Grosveld F, van Kuppeveld FJM, Haagmans BL, Enjuanes L, Drabek D, Bosch BJ. 2019. Towards a solution to MERS: protective human monoclonal antibodies targeting different domains and functions of the MERS-coronavirus spike glycoprotein. Emerg Microbes Infect 8:516-530.
76. de Wilde AH, Raj VS, Oudshoorn D, Bestebroer TM, van Nieuwkoop S, Limpens R, Posthuma CC, van der Meer Y, Bárcena M, Haagmans BL, Snijder EJ, van den Hoogen BG. 2013. MERS-coronavirus replication induces severe in vitro cytopathology and is strongly inhibited by cyclosporin A or interferon-α treatment. J Gen Virol 94:1749-1760.
77. Su B, Bettcher LF, Hsieh W-Y, Hornburg D, Pearson MJ, Blomberg N, Giera M, Snyder MP, Raftery D, Bensinger SJ, Williams KJ. 2021. A DMS Shotgun Lipidomics Workflow Application to Facilitate High-Throughput, Comprehensive Lipidomics. Journal of the American Society for Mass Spectrometry 32:2655-2663.
78. Ghorasaini M, Mohammed Y, Adamski J, Bettcher L, Bowden JA, Cabruja M, Contrepois K, Ellenberger M, Gajera B, Haid M, Hornburg D, Hunter C, Jones CM, Klein T, Mayboroda O, Mirzaian M, Moaddel R, Ferrucci L, Lovett J, Nazir K, Pearson M, Ubhi BK, Raftery D, Riols F,

995 Sayers R, Sijbrands EJG, Snyder MP, Su B, Velagapudi V, Williams KJ, de Rijke YB, Giera M.
996 2021. Cross-Laboratory Standardization of Preclinical Lipidomics Using Differential Mobility
997 Spectrometry and Multiple Reaction Monitoring. Analytical Chemistry 93:16369-16378.
998 79. Faas FG, Avramut MC, van den Berg BM, Mommaas AM, Koster AJ, Ravelli RB. 2012. Virtual
999 nanoscopy: generation of ultra-large high resolution electron microscopy maps. J Cell Biol
1000 198:457-69.

1001

1002 **Figure legends**

1003 **Figure 1**

1004 Gene expression of host factors of the DNL pathway increases upon MERS-CoV
1005 infection. A) Schematic representation of the main steps of the *de novo* lipogenesis
1006 pathway, the key enzymes involved (ACLY, ACC, FASN), and the downstream
1007 biological functions of the resulting fatty acids. Double arrows indicate that multiple
1008 reactions are involved but not depicted here. Small-molecule inhibitors used in this
1009 study are denoted in red. PTMs: posttranslational modifications. B) Gene expression
1010 analysis of key host factors participating in DNL and phospholipid synthesis (dark
1011 gray) or fatty acid oxidation (light gray) in mock-infected Huh7 cells in comparison
1012 with MERS-CoV-infected cells (MOI 5) at 12 h p.i. The mRNA levels of *ACLY, ACC,*
1013 *FASN, SCD-1, DGAT1, ADRP, CPT1a* and *ACOX* were determined by RT-qPCR
1014 and normalized against the mock-infected control. C) Western Blot analysis of ACC,
1015 phospho-ACC and FASN in MERS-CoV infected Huh7 cells, at 9 and 12 h p.i.
1016 Data are represented as mean ± SD of two biological replicates. Statistical
1017 significance was calculated using two-way ANOVA and applying Bonferroni multiple
1018 comparison correction, * $p<0.05$, ** $p< 0.01$, *** $p< 0.001$, **** $p< 0.0001$.

1019

1020 **Figure 2**

1021 DNL inhibition strongly reduces the release of infectious MERS-CoV progeny,
1022 without affecting intracellular viral RNA synthesis. A) Huh7 cells or B) MRC5 were

1023 infected with MERS-CoV (MOI 5) and treated with either DMSO (vehicle control) or
1024 10 μM TOFA from 1 h p.i. onward. Cell lysates were harvested at 12 h p.i. (Huh7
1025 cells) or 16 h p.i. respectively, and intracellular viral RNA copies were measured by
1026 RT-qPCR. C) and D) Infectious viral progeny was quantified by plaque assay on
1027 Huh7 cells, using the harvested culture supernatant (see panel A and B,
1028 respectively). E) Huh7 cells were infected with MERS-CoV (MOI 5) and treated with
1029 either DMSO (vehicle control) or 15 μM TVB-2640 from 1 h p.i. onward. At 16 h p.i.,
1030 cells were harvested, and intracellular viral RNA copies were measured by RT-
1031 qPCR. F) Infectious viral progeny from TVB-2640-treated and untreated Huh7 cells
1032 (see panel E) was quantified by plaque assay on Huh7 cells. G) Huh7 cells were
1033 infected with MERS-CoV (MOI 5) and treated with either DMSO (vehicle control) or
1034 10 μM TOFA from 1 h p.i. onward. Samples were collected at 12, 14, and 16 h p.i.
1035 Infectious viral progeny was quantified by plaque assay on Huh7 cells. While at 12 h
1036 p.i the number of infectious virus particles was below the detection limit of the assay,
1037 virus titers increased over time at 14 h p.i and 16 h p.i. H) Analysis of the secretory
1038 pathway's functionality upon TOFA treatment. Huh7 cells were transfected with a
1039 plasmid expressing *Gaussia* luciferase, a naturally secreted reporter protein. From 8
1040 h post transfection., transfected cells were treated with either 10 μM TOFA or 5 μM
1041 Brefeldin A. At 24 h post compound addition, the levels of extracellular *Gaussia*
1042 luciferase secreted in the supernatant were measured using an enzymatic assay
1043 (see Materials and Methods). I) The cell monolayers from the same wells (panel H)
1044 were also lysed and intracellular *Gaussia* luciferase expression was measured and
1045 compared with the amount of secreted reporter protein. Dotted lines indicate the
1046 background levels measured. Data are represented as mean ± SD of two (D), three
1047 (B, E, G) or four (H, I) biological replicates. Statistical significance was calculated

1048 using one-way ANOVA and applying Bonferroni multiple comparison correction, ***
1049 $p < 0.001$
1050
1051 **Figure 3**
1052 TOFA induces lipolysis in uninfected and MERS-CoV-infected cells.
1053 A) Uninfected Huh7 cells were treated with DMSO or 10 μM TOFA. B) Huh7 cells
1054 were infected with MERS-CoV (MOI 5) and treated with either DMSO (vehicle
1055 control) or 10 μM TOFA from 1 h p.i. onward. For both uninfected and infected cells,
1056 samples were collected at 8 and 11 h p.t. The next day the fixed cells were stained
1057 with BODIPY 493/503 (lipid droplets), and Hoechst 33342 (nuclei) and the presence
1058 of lipid droplets was analyzed by wide-field fluorescence microscopy.
1059
1060 **Figure 4**
1061 Subcellular localization of MERS-CoV envelope proteins following TOFA treatment.
1062 Huh7 cells were infected with MERS-CoV, treated with TOFA as previously
1063 described, fixed at 12 h p.i and analyzed using immunofluorescence microscopy.
1064 Cells were triple-labelled for A) S (green, panels i. and ii.) and or E proteins (green,
1065 panels iii. and iv.) in combination with labeling for giantin (red), as a marker for the
1066 Golgi complex or B) S (green, panels i. and ii.) and M (green, panels iii. and iv.)
1067 proteins in combination with labeling for giantin (red). Confocal images are
1068 representative of at least two independent biological replicates. White arrows point to
1069 co-localization foci of two or three markers.
1070
1071 **Figure 5**

1072 Effect of TOFA treatment on MERS-CoV structural protein expression and post-
1073 translational modifications. Expression levels of S protein (using separate antibodies
1074 against the S1 and S2 subunits), N protein, M protein, and E protein were analyzed
1075 by western blot, using β-actin as internal control. A) Huh7 cells were infected with
1076 MERS-CoV and treated with DMSO or TOFA as previously described. Supernatants
1077 were collected at 16 h p.i. and progeny virus particles were pelleted through a
1078 sucrose cushion by ultracentrifugation, lysed, and used for Western blot analysis. B)
1079 Huh7 cells were infected with MERS-CoV and DMSO- or TOFA-treated as
1080 previously described, and samples (WCL: Whole Cell Lysate) were collected at 9
1081 and 12 h p.i. for analysis by Western blotting. C) Western blot for PNGase assay
1082 (described in Materials and Methods) using lysates collected from MERS-CoV-
1083 infected Huh7 cells and collected at 12 h p.i. Blots are representative of at least two
1084 independent biological replicates.
1085
1086 **Figure 6**
1087 TEM analysis of TOFA-treated Huh7 cells infected with MERS-CoV. Cells were
1088 infected with MOI 5, treated with TOFA or with DMSO and fixed and processed for
1089 electron microscopy at 12 h p.i. A) Morphologically comparable virus-induced DMVs
1090 (asterisks) can be readily observed in both conditions. Close-ups of the boxed areas
1091 are provided in the insets. B) Extracellular virions abundantly present in the
1092 extracellular space of DMSO-treated MERS-CoV-infected cells (i, inset: zoomed-in
1093 image of the boxed area), but not in the extracellular space of TOFA-treated and
1094 virus-infected cells (ii). C) Consecutive stages of MERS-CoV particle assembly in
1095 DMSO-treated and infected cells; assembly events were split in two categories for
1096 simplicity (see Materials and Methods), denoted as early-stage assembly events of

1097 budding nucleocapsid complexes in membranes of the secretory pathway (panels i
1098 and ii) and late-stage assembly events including nearly fully-formed virus particles
1099 and virions fully-budded inside large vesicles (iii). D) In TOFA-treated MERS-CoV-
1100 infected cells early assembly stage events, as seen in panels (i) and (ii), were
1101 abnormally abundant, revealing a stalling of virus particle assembly in the presence
1102 of the compound. Mitochondria are annotated with M, convoluted membranes with
1103 CM, and cell nuclei with N. Scale bar is 200 nm.
1104
1105 **Figure 7**
1106 Exogenous palmitic acid supplementation partially rescues MERS-CoV assembly
1107 after TOFA treatment. A) Alignment of S and E protein C-terminal sequences from
1108 selected coronaviruses using the following accession numbers: MERS-CoV
1109 (NC_019843), SARS-CoV (NC_004718) SARS-CoV-2 (NC_045512), MHV
1110 (AY700211), TGEV (AJ271965), IBV (NC_001451), HCoV-229E (NC_001451).
1111 Cysteines next to the transmembrane domain that can serve as palmitoylation
1112 substrates are highlighted in yellow and noted with an asterisk. B) Huh7 cells were
1113 infected with MERS-CoV (MOI 5) and treated with either DMSO (vehicle control) or
1114 30 μM 2-BP from 1 h p.i. onward. At 16 h p.i., cell lysates were harvested, and
1115 intracellular viral RNA copies were measured by RT-qPCR. C) Infectious viral
1116 progeny was quantified by plaque assay on Huh7 cells. Data are represented as
1117 mean ± SD of three independent experiments. D) Huh7 cells were infected with
1118 MERS-CoV (MOI 5) and treated from 1 h p.i. onward with DMSO supplemented with
1119 100 μM BSA, TOFA, TOFA supplemented with 100 μM BSA-PA, or TOFA
1120 supplemented with 100 μM BSA-OA. At 16 h p.i., samples were collected, and
1121 infectious viral progeny was quantified by plaque assay on Huh7 cells. Data are

1122 represented as mean ± SD of two independent experiments. Statistical significance
1123 was calculated using one-way ANOVA and applying Dunnet multiple comparison
1124 correction, **** $p < 0.0001$ and ** $p < 0.01$, ns: not significant. E) Huh7 cells were
1125 infected with MERS-CoV and treated with DMSO, TOFA or TOFA with BSA-PA from
1126 1 h p.i. onward as previously described, and samples were collected at 12 h p.i. for
1127 analysis by western blotting. Blots are representative of at least two independent
1128 biological replicates. F-I) Huh7 cells were infected with MERS-CoV and treated as
1129 described above. At 12 h p.i., samples were fixed and processed for TEM. F) Post
1130 addition of palmitic acid, the number of extracellular virus particles present in TOFA-
1131 treated virus-infected cells is increased. Scale bar is 100nm. G) Virions either in the
1132 late-stage (advanced/ fully assembled particles) or early-stage were quantified (see
1133 Materials and Methods), and the ratio of both classes was determined. H) Number of
1134 DMVs per μm^2 of cytoplasm observed (see Materials and Methods) in the DMSO
1135 and BSA-treated, TOFA-treated or TOFA and BSA-PA-treated virus-infected cells. I)
1136 In the same samples, the area of CMs (in nm^2) was also determined per μm^2 of
1137 cytoplasm (see Materials and Methods). Data are represented as mean ± SD of
1138 three separate stiches. Statistical significance was calculated using one-way ANOVA
1139 and applying Tukey multiple comparison correction, *** $p < 0.001$, ** $p < 0.01$, and *
1140 $p<0.05$.

Figure 1

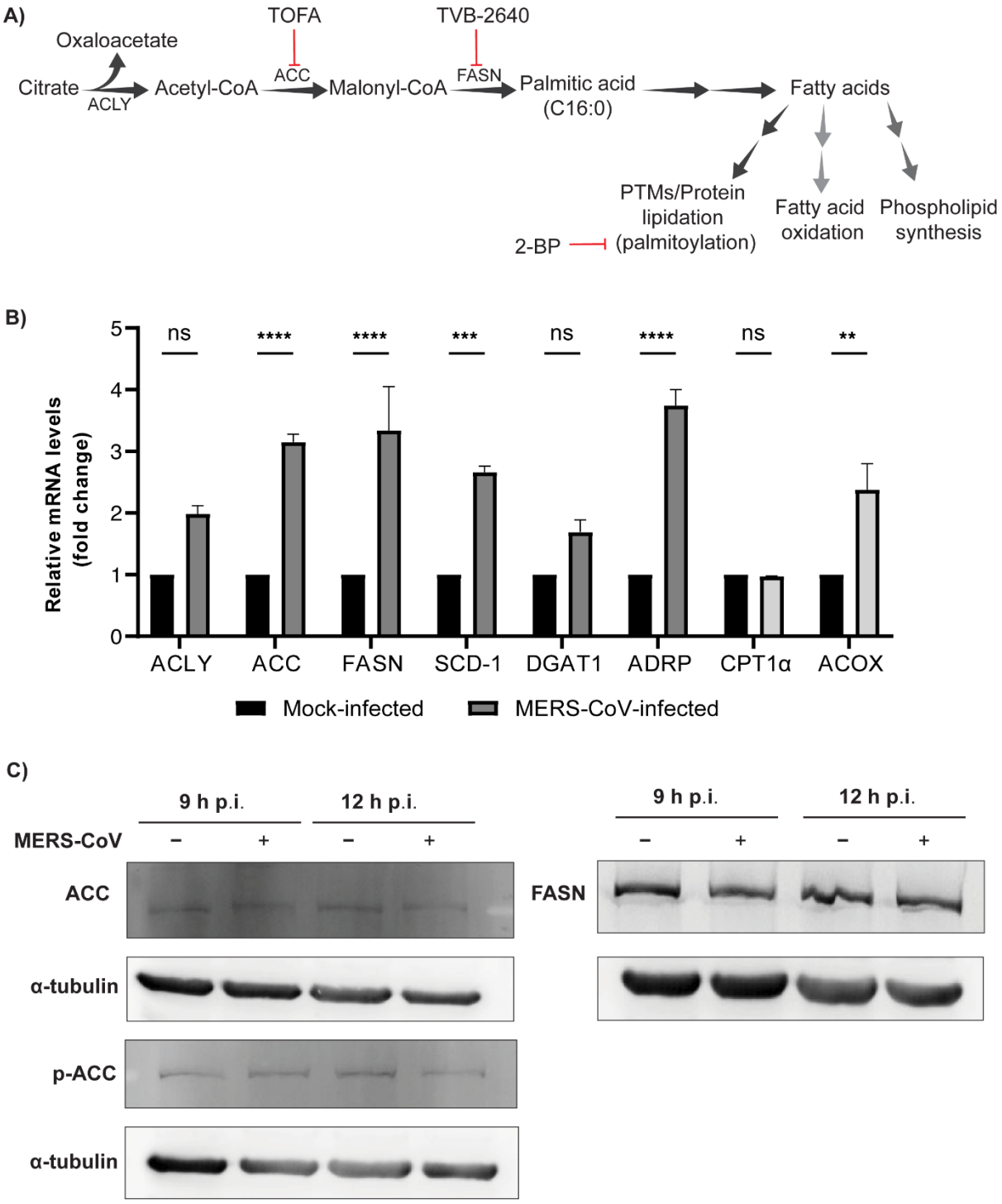
A)
Oxaloacetate
Citrate
ACLY
Acetyl-CoA
TOFA
ACC
Malonyl-CoA
TVB-2640
FASN
Palmitic acid
(C16:0)
Fatty acids
PTMs/Protein
lipidation
(palmitoylation)
2-BP
Fatty acid
oxidation
Phospholipid
synthesis
B)
Relative mRNA levels
(fold change)
0
1
2
3
4
5
ns
****
****
***
ns
****
ns
**
ACLY
ACC
FASN
SCD-1
DGAT1
ADRP
CPT1α
ACOX
Mock-infected
MERS-CoV-infected
C)
9 h p.i.
12 h p.i.
MERS-CoV
–
+
–
+
ACC
α-tubulin
p-ACC
α-tubulin
9 h p.i.
12 h p.i.
–
+
–
+
FASN

Figure 2

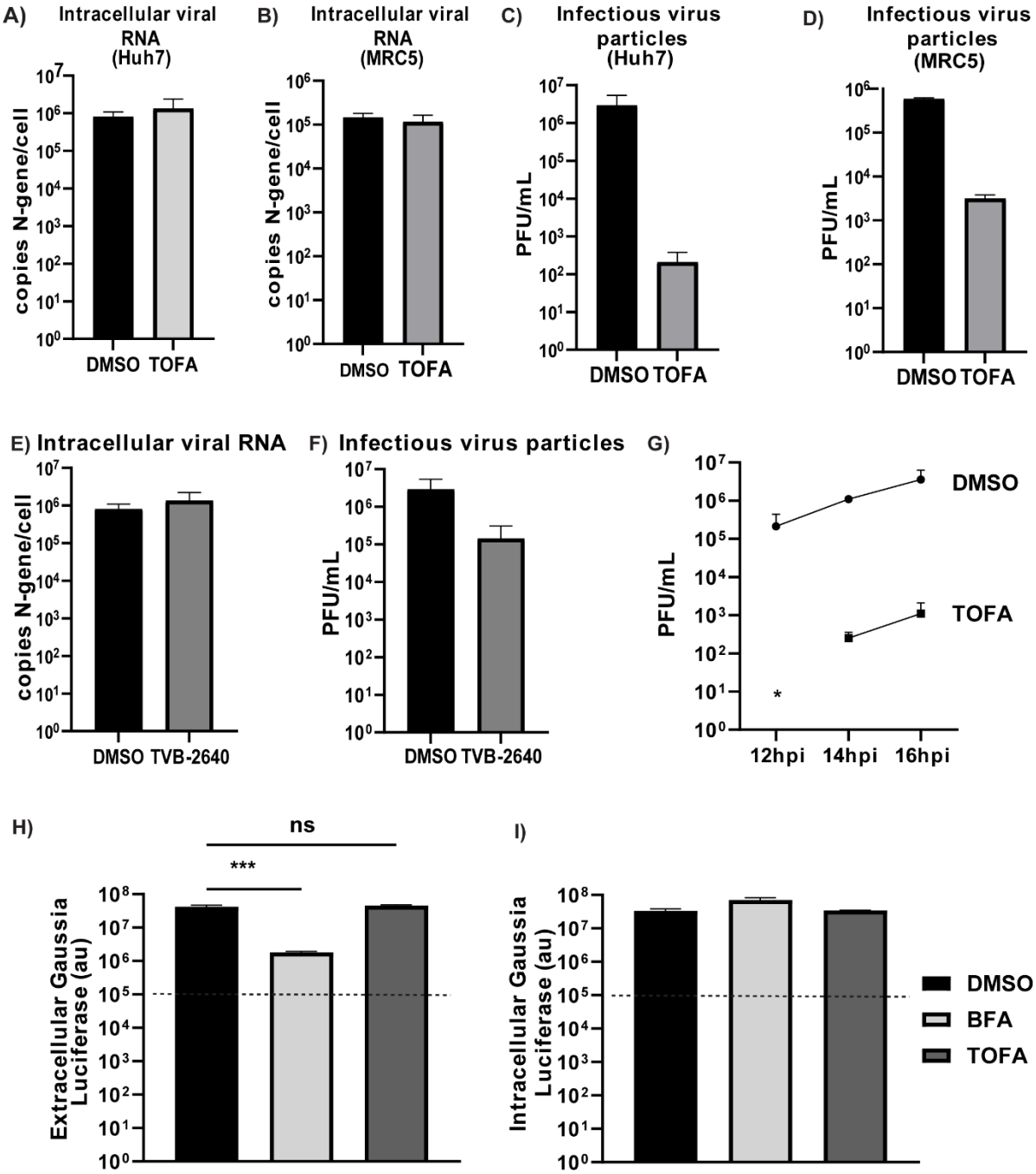
A)
Intracellular viral RNA (Huh7)
copies N-gene/cell
DMSO
TOFA
B)
Intracellular viral RNA (MRC5)
copies N-gene/cell
DMSO
TOFA
C)
Infectious virus particles (Huh7)
PFU/mL
DMSO
TOFA
D)
Infectious virus particles (MRC5)
PFU/mL
DMSO
TOFA
E) Intracellular viral RNA
copies N-gene/cell
DMSO
TVB-2640
F) Infectious virus particles
PFU/mL
DMSO
TVB-2640
G)
PFU/mL
DMSO
TOFA
*
12hpi
14hpi
16hpi
H)
ns
***
Extracellular Gaussia Luciferase (au)
I)
Intracellular Gaussia Luciferase (au)
DMSO
BFA
TOFA

Figure 3

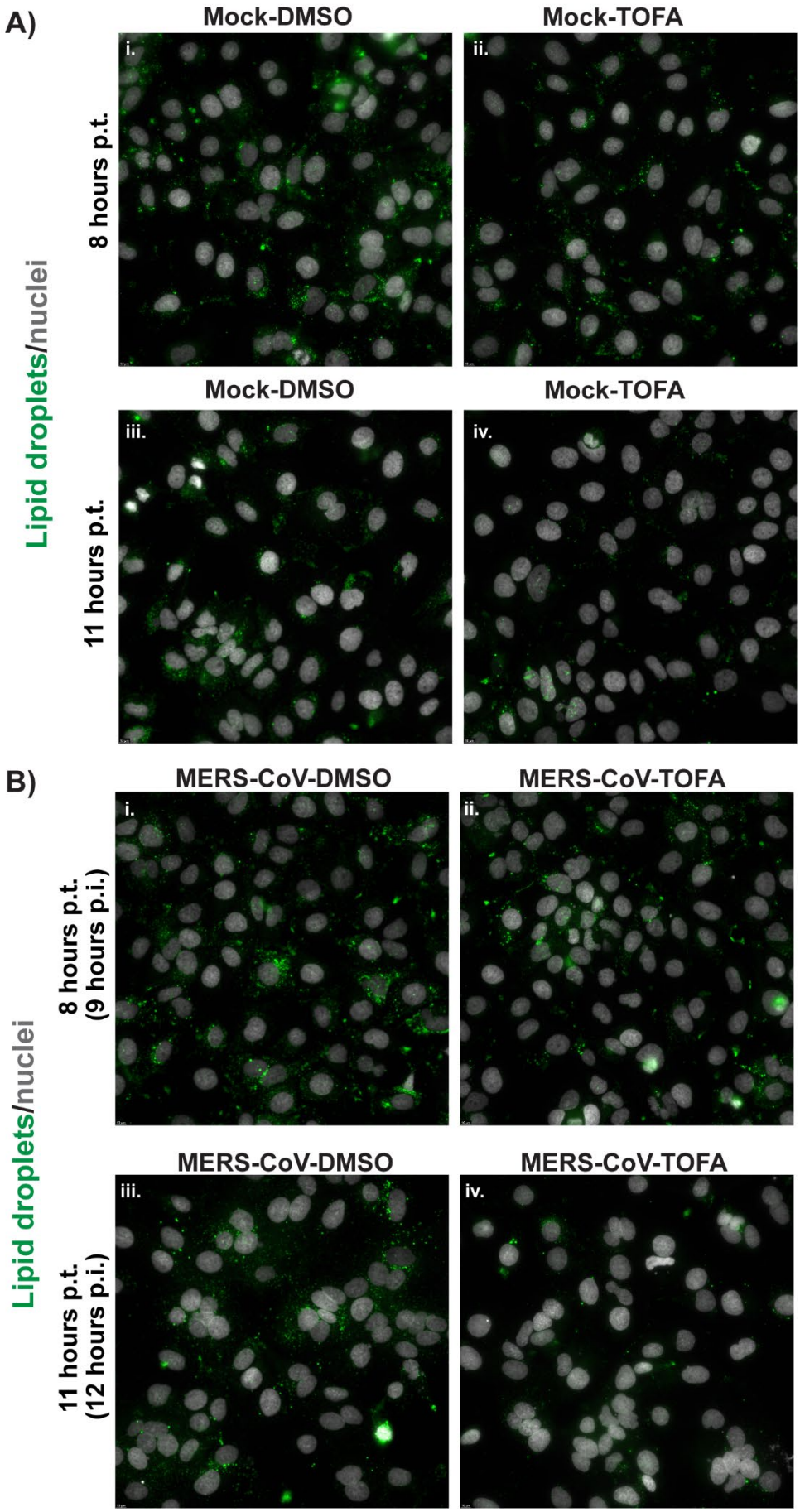
A)
Mock-DMSO
Mock-TOFA
i.
ii.
8 hours p.t.
Lipid droplets/nuclei
Mock-DMSO
Mock-TOFA
iii.
iv.
11 hours p.t.
B)
MERS-CoV-DMSO
MERS-CoV-TOFA
i.
ii.
8 hours p.t.
(9 hours p.i.)
Lipid droplets/nuclei
MERS-CoV-DMSO
MERS-CoV-TOFA
iii.
iv.
11 hours p.t.
(12 hours p.i.)

Figure 4

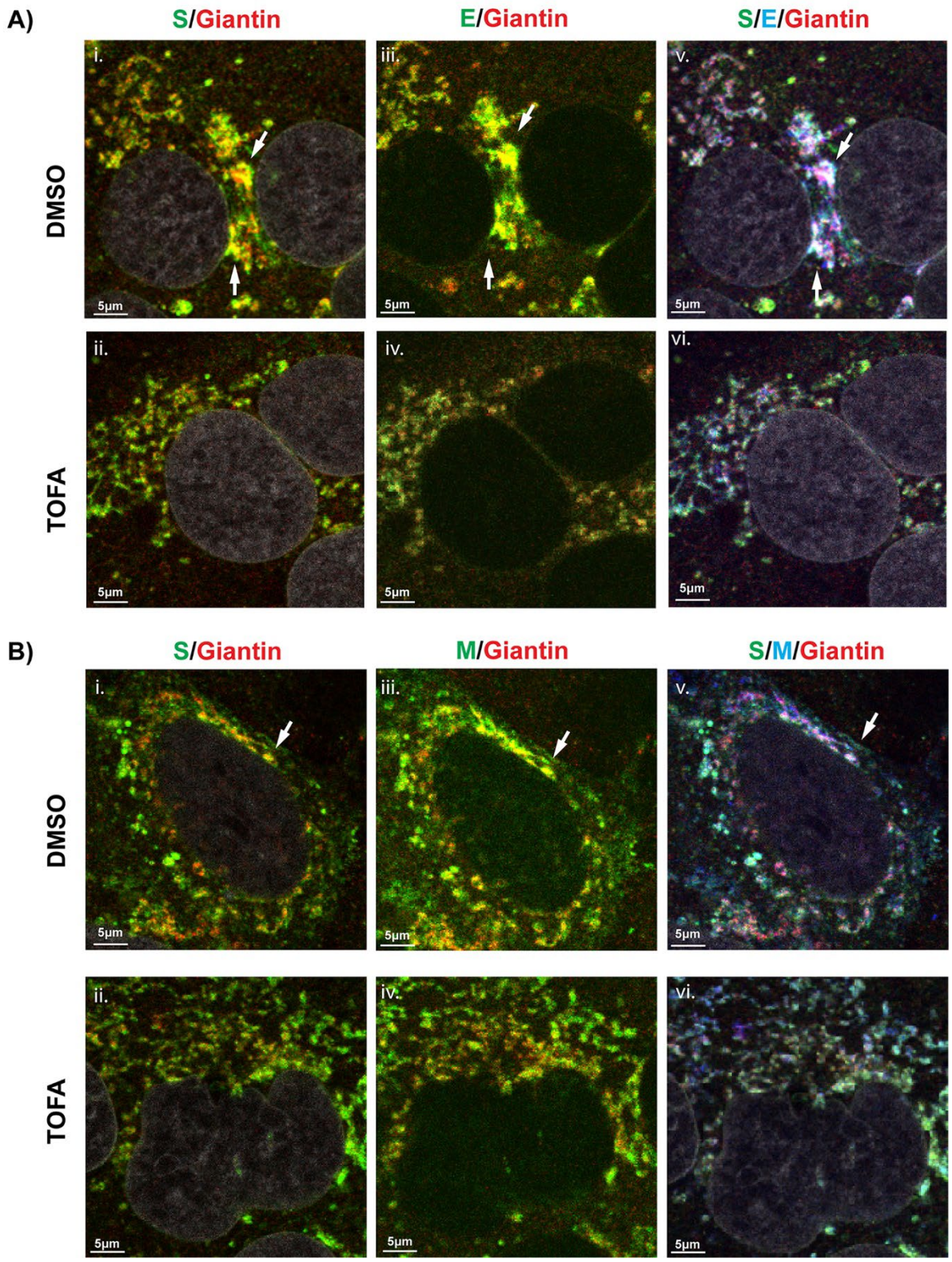
A)
S/Giantin
E/Giantin
S/E/Giantin
DMSO
TOFA
i.
ii.
iii.
iv.
v.
vi.
5µm
B)
S/Giantin
M/Giantin
S/M/Giantin
DMSO
TOFA
i.
ii.
iii.
iv.
v.
vi.
5µm

Figure 5

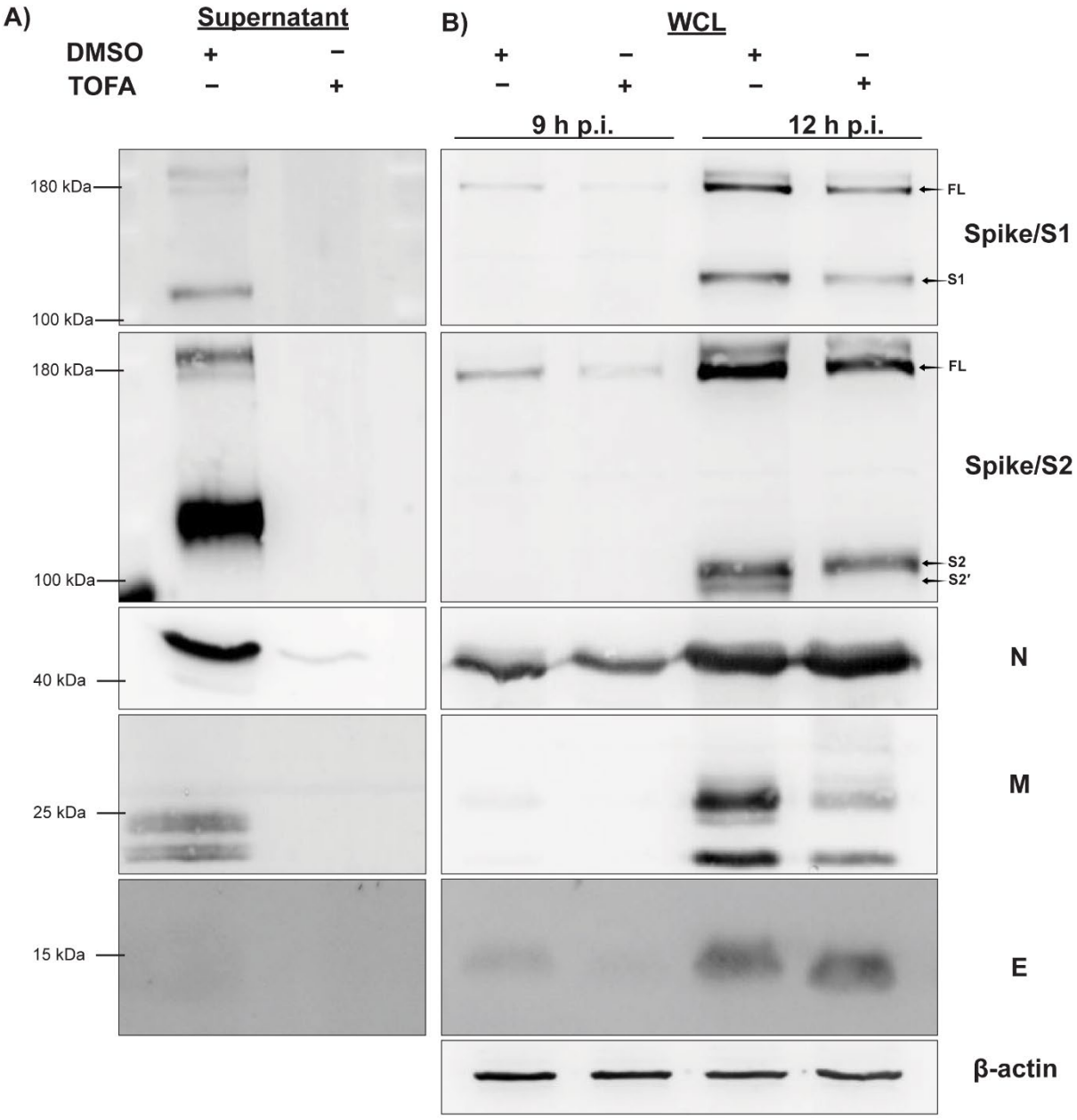
A)
Supernatant
DMSO + −
TOFA − +
B)
WCL
+ − + −
− + − +
9 h p.i.
12 h p.i.
180 kDa
100 kDa
FL
S1
Spike/S1
180 kDa
100 kDa
FL
Spike/S2
S2
S2′
40 kDa
N
25 kDa
M
15 kDa
E
β-actin

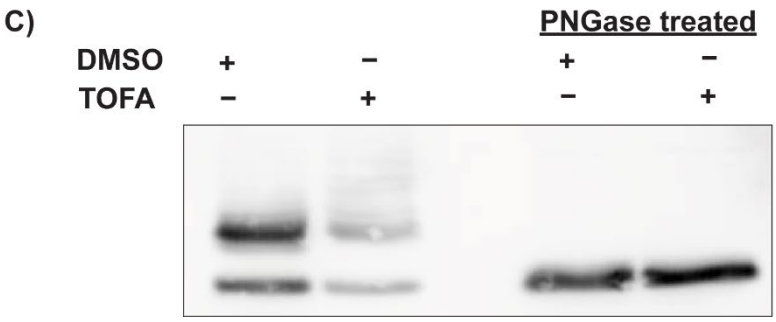
C)
PNGase treated
DMSO + − + −
TOFA − + − +

Figure 6

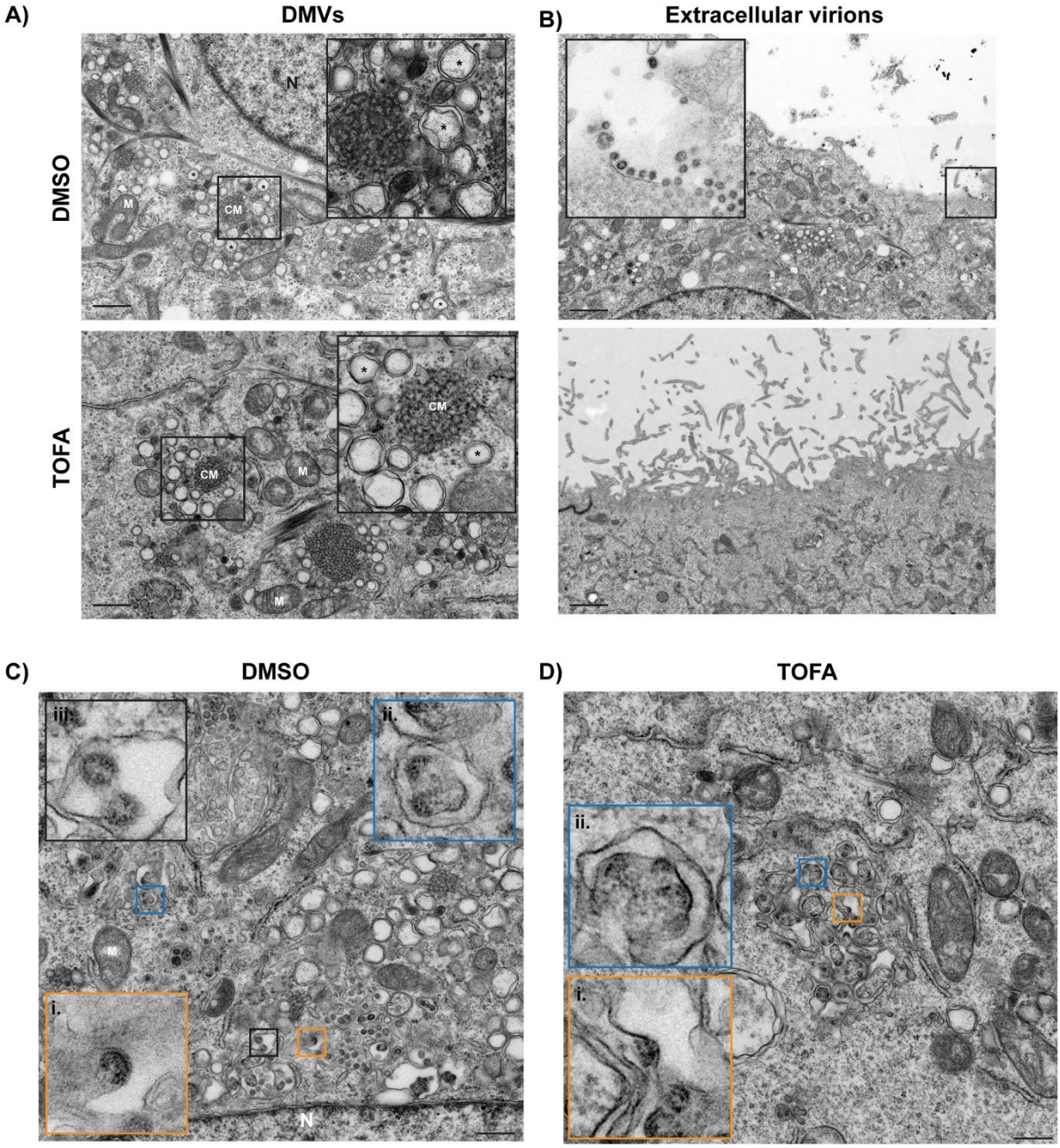
A)
DMVs
B)
Extracellular virions
DMSO
TOFA
N
M
CM
C)
DMSO
D)
TOFA
i.
ii.
iii.

Figure 7

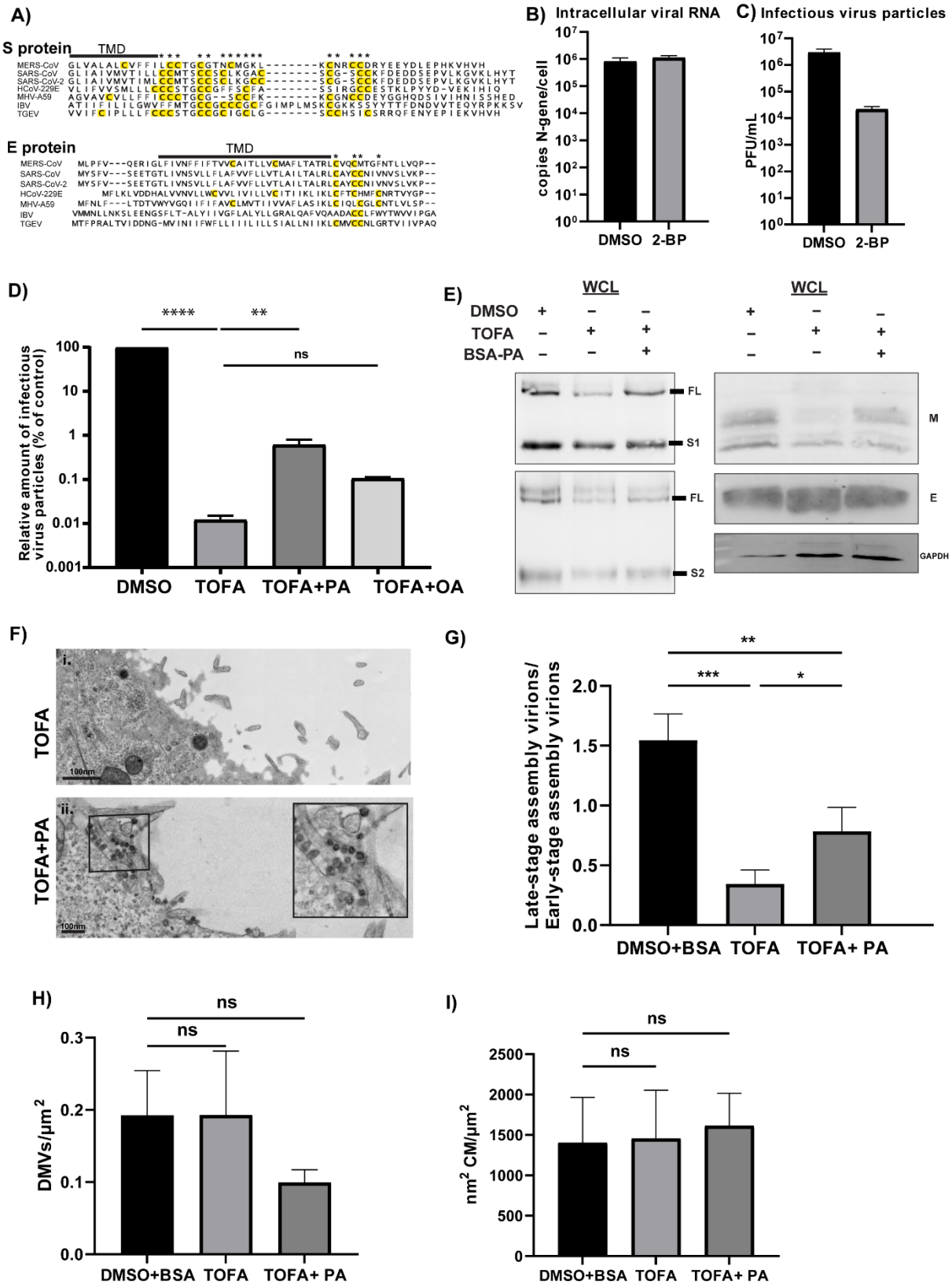
A)
S protein
TMD
MERS-CoV
SARS-CoV
SARS-CoV-2
HCoV-229E
MHV-A59
IBV
TGEV
E protein
TMD
B) Intracellular viral RNA
copies N-gene/cell
DMSO
2-BP
C) Infectious virus particles
PFU/mL
DMSO
2-BP
D)
Relative amount of infectious virus particles (% of control)
****
**
ns
DMSO
TOFA
TOFA+PA
TOFA+OA
E)
WCL
WCL
DMSO
TOFA
BSA-PA
FL
S1
FL
S2
M
E
GAPDH
F)
TOFA
TOFA+PA
i.
ii.
100nm
100nm
G)
Late-stage assembly virions/ Early-stage assembly virions
**
***
*
DMSO+BSA
TOFA
TOFA+ PA
H)
DMVs/µm²
ns
ns
DMSO+BSA
TOFA
TOFA+ PA
I)
nm² CM/µm²
ns
ns
DMSO+BSA
TOFA
TOFA+ PA